



LADAR RANGE IMAGE INTERPOLATION
EXPLOITING PULSE WIDTH EXPANSION

THESIS

Second Lieutenant Jeramy W. Motes,

AFIT/GE/ENG/12-30

DEPARTMENT OF THE AIR FORCE
AIR UNIVERSITY

AIR FORCE INSTITUTE OF TECHNOLOGY

Wright-Patterson Air Force Base, Ohio

APPROVED FOR PUBLIC RELEASE; DISTRIBUTION UNLIMITED.

The views expressed in this thesis are those of the author and do not reflect the official policy or position of the United States Air Force, Department of Defense, or the United States Government. This material is declared a work of the U.S. Government and is not subject to copyright protection in the United States.

LADAR RANGE IMAGE INTERPOLATION
EXPLOITING PULSE WIDTH EXPANSION

THESIS

Presented to the Faculty
Department of Electrical and Computer Engineering
Graduate School of Engineering and Management
Air Force Institute of Technology
Air University
Air Education and Training Command
In Partial Fulfillment of the Requirements for the
Degree of Master of Science in Electrical Engineering

Second Lieutenant Jeramy W. Motes, B.S.E.E.

March 2012

APPROVED FOR PUBLIC RELEASE; DISTRIBUTION UNLIMITED.

LADAR RANGE IMAGE INTERPOLATION
EXPLOITING PULSE WIDTH EXPANSION

Second Lieutenant Jeramy W. Motes, B.S.E.E.

Approved:

/signed/

9 Mar 2012

Dr. Richard Martin (Chairman)

date

/signed/

9 Mar 2012

Dr. Stephen Cain (Member)

date

/signed/

9 Mar 2012

Dr. Julie Jackson (Member)

date

Abstract

Laser Detection and Ranging (LADAR) systems produce both a range image and an intensity image by measuring the intensity of light reflected off a surface target. When the transmitted LADAR pulse strikes a sloped surface, the returned pulse is expanded temporally. This characteristic of the reflected laser pulse enables the possibility of estimating the gradient of a surface. This study estimates the gradient of the surface of an object from a modeled LADAR return pulse that includes accurate probabilistic noise models. The range and surface gradient estimations are incorporated into a novel interpolator that facilitates an effective *three dimensional* (3D) reconstruction of an image given a range of operating conditions. The performance of the novel interpolator is measured by comparing the reconstruction effort against the performance of three common interpolation techniques: linear, spline, and sinc.

Acknowledgements

First, I would like to thank my thesis advisor, Dr. Richard Martin. Without his guidance and support throughout this research effort I would not have been able to complete it. The technical expertise and advice proved to be a guiding light, leading me on the path to academic success.

I would also like to thank my friends for which I had the pleasure of sharing this enlightening experience with. I could not have accomplished my goals without your help. I would also like to acknowledge and express the highest order of compliments to the few who powered through the dark nights along side me in the optics lab.

Finally I would like to thank my wife and children for their support. Your love and affection kept me balanced and provided me the fuel necessary to finish this race.

Second Lieutenant Jeramy W. Motes

Table of Contents

	Page
Abstract	iv
Acknowledgements	v
Table of Contents	vi
List of Figures	ix
List of Tables	xi
List of Abbreviations	xii
I. Introduction	1
1.1 Background	1
1.2 Research Goals	3
1.3 Assumptions	3
1.4 Related Research	4
1.5 Thesis Organization	4
II. Problem Background	6
2.1 3D LADAR Model	6
2.1.1 Laser Pulse Generation	7
2.1.2 Light Propagation	10
2.1.3 Laser Beam Target Interaction	12
2.1.4 Pulse Width Expansion	14
2.1.5 Target Dependent Characteristics	15
2.1.6 Range Equation	16
2.1.7 Noise Modeling	17
2.1.8 Detector Characteristics	19
2.2 Interpolation	20
2.2.1 Linear Interpolation	20
2.2.2 Sinc Interpolation	21
2.2.3 Spline Interpolation	22
2.2.4 Hermite Interpolation	23
2.3 Sampling	24
2.3.1 Time Domain Sampling Constraint	25
2.3.2 Spatial Domain Sampling Constraints	26
2.4 Estimation Theory	27
2.5 Chapter Summary	28

	Page
III. Research Methodology	29
3.1 Parameters of LADAR Model	29
3.1.1 Spatial Sampling Constraints	32
3.2 3D LADAR Model	34
3.2.1 Development of 3D Gaussian Beam at Target Plane	34
3.2.2 Beam Target Interaction	37
3.2.3 Additive Noise	39
3.2.4 Exclusion of Atmospheric and Optical Aberrations	42
3.3 Estimation	42
3.3.1 Angle Estimation Reasoning	44
3.4 Interpolation	44
3.5 Testing Effort	47
3.5.1 Target Creation and Down Sampling Implemen-	
tation	47
3.5.2 Root Mean Square Error	48
3.5.3 T-test	48
3.5.4 Survey	50
3.5.5 LADAR Model Adjustments	51
3.6 Chapter Summary	52
IV. Results and Analysis	53
4.1 Survey Results	53
4.1.1 Resiliency of Interpolators	56
4.2 Hypothesis Testing	59
4.3 General RMSE Results	60
4.3.1 Target RMSE Analysis	60
4.3.2 Time Sampling Rate RMSE Analysis	62
4.4 Adjustment of Bi-Hermite Algorithm	65
4.5 Estimation Error	69
4.5.1 Target Estimation MAE Analysis	69
4.5.2 Time Sampling Rate Estimation MAE Analysis	70
4.5.3 FWHM Estimation MAE Analysis	72
4.6 Mitigation of Pulse Width Expansion Error	75
V. Conclusions and Future Work	76
5.1 Conclusions	76
5.1.1 Hermite Interpolator Performance	76
5.1.2 Ideal LADAR Operating Conditions	76
5.2 Future Work	77
5.2.1 Experimental Results	77

	Page
5.2.2 LADAR Model Complexity	77
5.2.3 Different LADAR Applications	78
5.2.4 Different Image Processing Applications	78
5.2.5 Test Over Ranges	78
5.2.6 Thoroughly Test Hermite Interpolator	78
Appendix A. Human Subject Paperwork	79
Bibliography	85

List of Figures

Figure		Page
2.1.	The components of the LADAR simulation.	7
2.2.	Shows three of the laser pulse temporal profiles that were considered for this study.	8
2.3.	Gaussian pulse model with identical parameters with the exception of τ_g	9
2.4.	Three dimensional interpolation of one pixel. The pixel value represents the height of an object in this study.	20
2.5.	The 2D sinc filter. The sampling interval for the sinc filter is $1/4$	22
2.6.	The two dimensional interpolation comparison between the cubic spline and cubic Hermite.	25
3.1.	Target profiles.	33
3.2.	The Gaussian beam upon exiting the laser cavity of the LADAR.	35
3.3.	Two Gaussian beams with different beam waists.	36
3.4.	Comparison of Gaussian pulse interaction with two different target slopes.	38
3.5.	Noise functions.	40
3.6.	Noise comparison.	41
3.7.	The 28 by 28 grid of sampled points is interpolated by a factor of two for comparison to the original image with a resolution of 56 by 56.	45
4.1.	Control images related to survey and RMSE plots in Figures 4.3 through 4.6.	55
4.2.	One set of interpolated images included in the survey.	55
4.3.	Target 4 (Multi-Cone) results.	56
4.4.	Target 6 (Multi-Square) results.	57
4.5.	Target 8 (Multi-Trap) results.	57
4.6.	Target 9 (Multi-Shape) results.	58

Figure		Page
4.7.	LR interpolator RMSE comparisons across all nine targets. . .	61
4.8.	SLR interpolator RMSE comparisons across all nine targets. . .	61
4.9.	LR Hermite interpolator RMSE average plotted against the sampling rate in the time domain.	63
4.10.	LR linear interpolator RMSE average plotted against the sampling rate in the time domain.	64
4.11.	LR spline interpolator RMSE average plotted against the sampling rate in the time domain.	64
4.12.	LR sinc interpolator's RMSE average plotted against the sampling rate.	65
4.13.	The RMSE of each scaling factor of the Hermite function concerning the magnitude of the gradient.	67
4.14.	RMSE comparison between the Hermite algorithm that used slope angle and the Hermite algorithm that used the scaled magnitude of the slope of the target.	68
4.15.	Interpolation of target nine using SLR estimates and the bi-Hermite algorithm using radians for magnitude.	68
4.16.	Interpolation of target nine using SLR estimates and the bi-Hermite algorithm using the tangent of radians scaled by 0.25 for magnitude.	69
4.17.	Shows average MAE of angle estimations for LR and SLR tests against each target profile.	71
4.18.	Shows average MAE of range estimations for LR and SLR tests against each target profile.	71
4.19.	Shows error of angle estimation for LR and SLR tests against the Nyquist sampling scale.	72
4.20.	Shows error of range estimation for LR and SLR tests against the Nyquist sampling scale.	73
4.21.	Shows error of angle estimation for FWHM (τ_g) tests against the Nyquist sampling scale.	73
4.22.	Shows error of range estimation for FWHM (τ_g) tests against the Nyquist sampling scale.	74

List of Tables

Table		Page
3.1.	Constant system specifications of the LADAR.	30
3.2.	Variable system specifications of the LADAR model.	31
3.3.	The search space angles of the target's slope.	44
3.4.	Variable parameters of LADAR simulation dictated by the range to target.	52
4.1.	Target reference table.	53
4.2.	Human subject survey results.	54
4.3.	RMSE results. Percentages are rounded to nearest integer. . . .	54
4.4.	Mean of the difference in RMSE between ideal and actual esti- mation performance.	58
4.5.	Hypothesis test at range to target of 10 kilometers.	59
4.6.	Shows the averaged RMSE values of each interpolator against each constructed target used in the simulations.	62
4.7.	Shows the averaged RMSE values of each interpolator using SLR spatial sampling estimates against the different sampling rates in the time domain.	63

List of Abbreviations

Abbreviation		Page
LADAR	Laser Detection and Ranging	1
3D	Three Dimensional	2
ATR	Automatic Target Recognition	2
FWHM	Full-Width Half Maximum	8
TEM	Transverse Electric and Magnetic	9
BRDF	Angle Resolved Bidirectional Reflection Distribution . . .	13
FOV	Field of View	17
APD	Avalanche Photo Diode	18
SNR	Signal to Noise Ratio	19
2D	Two Dimensional	20
RMSE	Root Mean Square Error	23
LR	Low Resolution	31
SLR	Super Low Resolution	31
SD	Standard Deviation	60
MAE	Mean Absolute Error	69

LADAR RANGE IMAGE INTERPOLATION

EXPLOITING PULSE WIDTH EXPANSION

I. Introduction

This chapter describes the problem to be addressed by this research. Background of the problem and goals for this research are given, as well as assumptions used to limit the scope of the research. Previous related research is provided as well as the organization for the rest of the thesis.

1.1 *Background*

Laser Detection and Ranging (LADAR) is an optical remote sensing technology that uses lasers to sense the location of distant objects. LADAR is very similar to radar and they operate on the same basic foundation. Radar and LADAR operate on the premise of measuring the time of flight that it takes the transmitted energy to travel to and reflect back to a receiver. The difference between the two technologies is the wavelength of radiation that are used to sense targets. LADAR uses a wavelength on the order of micro meters or smaller. The small wavelength characteristic permits LADAR to consistently image targets with sub meter accuracy, an advantage over radar. The ability to resolve images with sub meter accuracy lends this technology to the applications for which LADAR is utilized. Some of these applications include environmental mapping, navigation and guidance, target recognition, and several more military applications.

Military applications of LADAR consist of ranging, tracking, target recognition, and mapping. These applications using LADAR enable the possibility of terrain mapping, obstacle avoidance, and smart guidance of munitions [1]. The military is currently developing a program that uses data generated by a LADAR camera on a delivery vehicle in real time to identify high value targets and adjust course as

necessary. The delivery vehicle scans objects using LADAR while flying in a loitering pattern. The 3D range images generated from the LADAR scans are compared against stored images in a target recognition effort. Increasing the resolution of the returned data would be desirable because it would increase the accuracy of the *automatic target recognition* (ATR) process [2]. In addition, before final orders are confirmed, a human in the decision process loop will confirm the results of the ATR.

One way to increase resolution of an image is to use an interpolator. Interpolation is the process of filling in new data values between known data points [3]. There are several interpolators available that are utilized to increase the resolution of a detected image. Typical interpolation is conducted with the linear [4], spline [5], and sinc [6] interpolators, which present an adequate ability to estimate the data points between measured points. These interpolators are limited because they rely on only one set of data information, the ranges to the target for each pixel. A Hermite interpolator would be preferred [7], but it relies on two sets of information, the ranges to the target and the target's surface gradients. To use a Hermite interpolator, additional information about the target is required. Fortunately, this information can be found in the LADAR return.

3D LADAR systems produce both a range image and an intensity image. When the transmitted LADAR pulse strikes a sloped surface, the returned pulse is expanded [8], [9]. This makes it possible to estimate the magnitude of the gradient of a surface, pixel by pixel. In LADAR-based target recognition, low resolution is often more of a limiting factor than noise, hence it is desirable to exploit all information available to increase the resolution of the range image. Moreover, in some LADAR systems, multiple pulse returns can be distinguished and processed. For the scope of this research, only single pulse returns will be studied.

Previous work on LADAR pulse width expansion has dealt with either characterizing the pulse width expansion and using it to increase the range accuracy in the longitudinal dimension [8], or computing performance bounds on the effect the pulse

width expansion has on the longitudinal range resolution [9]. In contrast, this study takes advantage of additional information contained in the pulse width expansion to improve angular resolution of the range image in the two transverse dimensions (i.e. the two dimensions perpendicular to the laser transmission, which is in the longitudinal dimension) by using a Hermite interpolator.

There are two types of LADAR systems, direct-detection LADAR and coherent LADAR [10]. Direct-detection LADAR transmits a single laser pulse that illuminates the target and records the energy received from the reflected pulse. Each pixel in a direct-detection LADAR records a small piece of the reflected light and the range is estimated for the object in its field of view. When all of the pixels across a detector are combined, a 3D image can be constructed. A coherent LADAR system sends out a signal on a carrier frequency, generally using optical heterodyne detection. A coherent detection system is often more complex than a direct-detection LADAR and requires the use of diffraction-limited optics to achieve efficiency [11]. Because of these limitations, direct-detection LADAR is used for this study.

1.2 Research Goals

The primary goal of this research is to prove that the pulse width expansion in a LADAR return is measurable and can be effectively utilized to enhance the image quality of an observed target. This is proven by estimating the gradient of the surface of the object derived by the significance of the pulse width expansion when compared to the original transmitted pulse width in the temporal domain. The gradient characterization of the object, along with the range information, are utilized by a Hermite interpolator to increase the angular resolution of an image more accurately than existing interpolators.

1.3 Assumptions

For this research, the following assumptions were made:

- The pulse generated by the transmitter is Gaussian in both temporal and spatial dimensions.
- The LADAR transmitter and detector are normal to the target plane.
- The target consists entirely of rough surfaces, and the reflection coefficient for the entire target object space is the same.
- The LADAR optics induced aberrations on the reflected light are negligible.
- The atmospheric effects on the propagation of light are negligible due to the assumed favorable conditions in which the LADAR is operated.

1.4 *Related Research*

Previous work on LADAR pulse width expansion has dealt with either characterizing the pulse width expansion and using it to increase the range accuracy in the longitudinal dimension [8], [12], computing performance bounds on the effect the pulse width expansion has on the longitudinal range resolution [9], or deriving the surface slope of a target based on range estimates [12]. In contrast, this study takes advantage of the additional information contained in the pulse width expansion to improve the angular resolution of the range image in the two transverse dimensions (the two dimensions perpendicular to the laser transmission) through the use of a Hermite interpolator.

1.5 *Thesis Organization*

Chapter II provides a description of the LADAR model, including the transmitted pulse, the propagation of the pulse, and the noise effects. In addition, Chapter II covers sampling, interpolation, and estimation theory. Chapter III explains the novel aspects of the LADAR model and the Hermite interpolation algorithm, as well as the methodology used in developing tests for this research. Chapter IV details the results from the simulations described in Chapter III. Finally, Chapter V gives a summary of

the research and lists conclusions of the thesis as well as potential follow-on research areas.

II. Problem Background

This study relies heavily on an accurate representation of a LADAR system. Therefore, considerable effort is spent explaining the components which sum together to create the LADAR system model. This study also implements estimation algorithms to quantify range and pulse width expansion significance as well as several signal processing techniques to measure and process the data. The algorithms and techniques chosen are described. This chapter provides a foundation of understanding, which is needed to analyze and explain the test process and results from this study.

The explanation of the 3D direct detection LADAR model utilized for simulation will be simplified by subdividing the model into logical sections. Each section will discuss the motivation and reason behind its function. Once the model is established, the processing techniques relating to the focus of this research are expounded upon.

2.1 3D LADAR Model

The explanation of the LADAR model begins with the transmission of laser light. The transmission of laser light includes the pulse model and the propagation of the light through a medium. A few pulse models are shown, with one being ultimately selected. The light propagation is explained by utilizing a general model. The next logical step is the object interaction with the propagated laser pulse that originated from the LADAR system. The object interaction with the pulse is very complicated, therefore, assumptions will be presented and justified to simplify the model. The object interaction is the capital section of the LADAR model because it explains the exploited characteristic of the reflected laser pulse. The range equation is incorporated into the model to determine the power received from the laser reflection off the target. Next, the noise sources in the system are described and broken down into three different models. The LADAR model description is completed by explaining the type of detector used and its behavioral properties. A process flow model of the LADAR simulation components is shown in Figure 2.1.

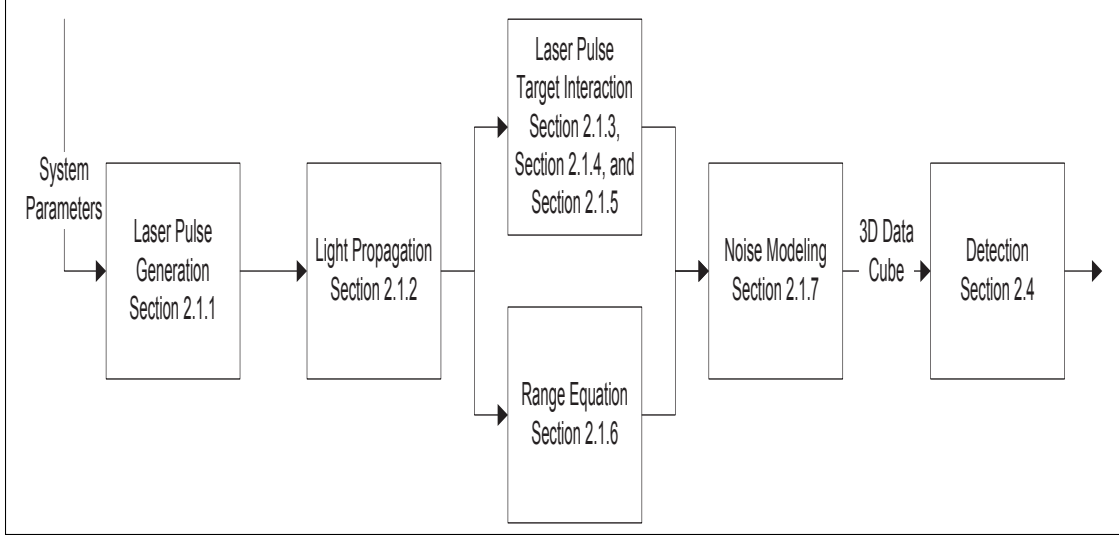


Figure 2.1: The components of the LADAR simulation.

Before further description of the LADAR model is elaborated, this paper defines the use of the following words for clarity. The word ‘beam’ refers to the spatial and 3D profile of the light. The word ‘pulse’ is used to describe the laser profile in the time domain.

2.1.1 Laser Pulse Generation. This section describes the characteristics of a laser beam generator along with the light propagation properties. The laser generator is described by the power output and the laser beam profile. The possible models for light pulses are presented, with one model selected for the study. The propagation of the light will be explained to conclude the section.

The light source in a LADAR system is a laser. Pulse lasers can be described by their average power in Watts. They can be further reduced into energy per pulse with the unit of measure in Joules. Laser sources can be described as a volumetric energy distribution in three dimensions, which are deconstructed into temporal and spatial domains.

A laser pulse description includes characteristics in multiple domains. Each domain description is independent of each other. There are several models that are used to describe a laser pulse. For the longitudinal or temporal domain, models

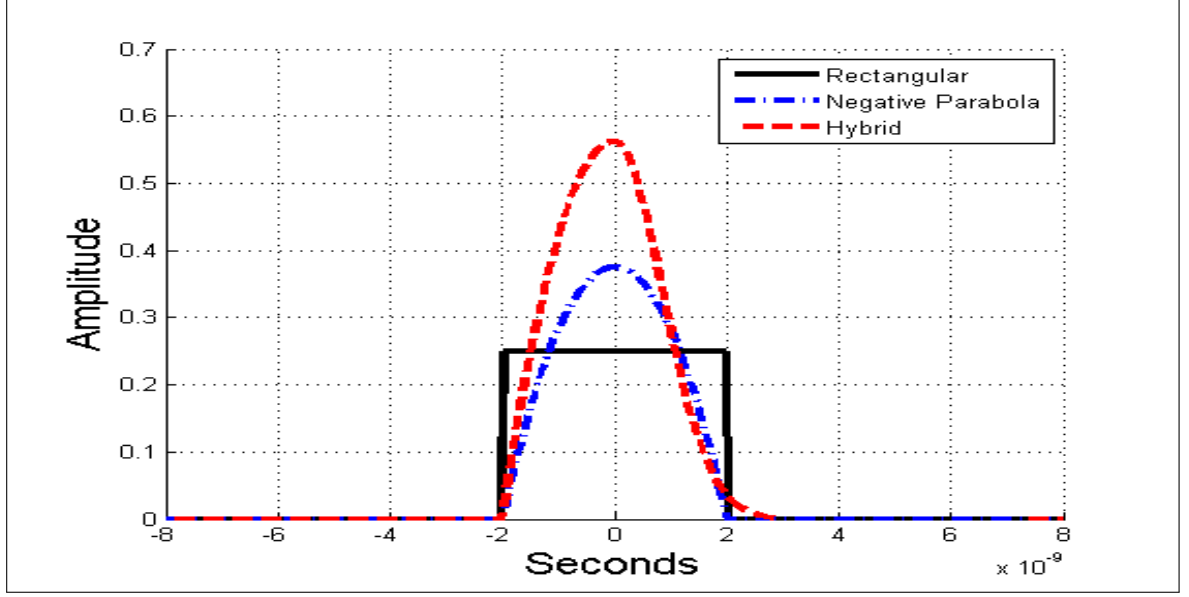


Figure 2.2: Shows three of the laser pulse temporal profiles that were considered for this study.

include the rectangle, the negative parabolic, Gaussian, and hybrid pulse models. The pulse temporal profiles of the rectangle, negative parabolic, and hybrid models are shown in Figure 2.2. Due to its combination of accuracy and ease of use, the Gaussian pulse was chosen by the author to describe the laser in the temporal domain. The laser pulse temporal profile is calculated by [11]

$$P_t(t) = \frac{E_t}{\sigma_w \sqrt{2\pi}} \exp \left[\frac{-(t)^2}{2\sigma_w^2} \right], \quad (2.1)$$

where $P_t(t)$ is the power of the laser pulse in units of watts, E_t is the energy of the pulse in Joules, and σ_w is the standard deviation of the Gaussian pulse. The value of the standard deviation of the Gaussian pulse is defined by the *full-width half-maximum* (FWHM), a metric used to describe the width or duration of a pulse. The FWHM represents the width of the Gaussian pulse when the pulse is half of what the maximum value of it is. The standard deviation of a Gaussian beam is derived by the

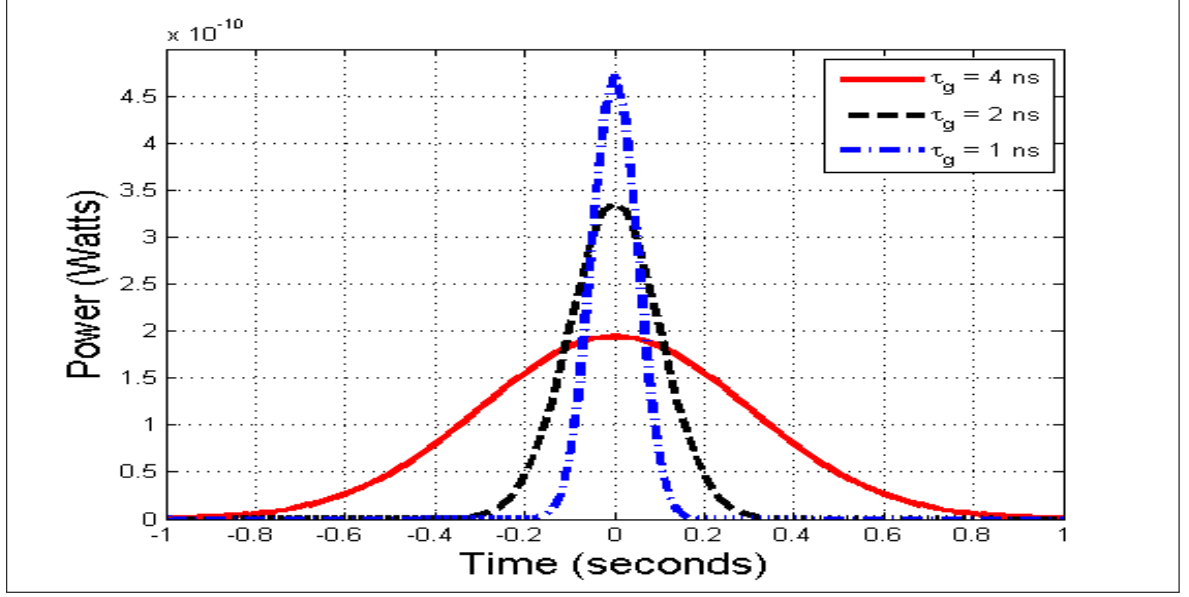


Figure 2.3: Gaussian pulse model with identical parameters with the exception of τ_g .

desired FWHM, shown by [9]

$$\sigma_w = \frac{\tau_g}{\sqrt{8\ln(2)}}, \quad (2.2)$$

where τ_g represents the FWHM, typically specified on the order of nanoseconds. The FWHM is important in defining a Gaussian beam because 63% of the energy in a Gaussian laser pulse is within this boundary. The FWHM significance in the generation of the Gaussian pulse is shown by Figure 2.3. Increasing the size of the FWHM of a Gaussian pulse decreases the amplitude. The inverse relationship of the amplitude of the Gaussian pulse and its FWHM size is driven by the total power in each pulse, in this instance 1 nW.

The first description of the laser pulse detailed the characteristics of the laser in the temporal domain. For the transverse domain, lasers are classified by the *transverse electric and magnetic* (TEM) mode. One of the most widely used modes for lasers is the TEM_{00} mode, known for its Gaussian profile [14]. The Gaussian function is utilized again to describe the energy distribution of the laser beam in the spatial or

transverse domain. For this mode, the two dimensional Gaussian beam exiting the laser beam cavity is [11]

$$g(x, y) = \frac{1}{2\pi\omega_o^2} \exp\left(\frac{-x^2}{2\pi\omega_o^2}\right) \exp\left(\frac{-y^2}{2\pi\omega_o^2}\right), \quad (2.3)$$

which describes the distribution of the field before it is implemented into a propagation function. The field is normalized by multiplying it by the inverse of the square root of the squared sum of the field. The field, $g(x, y)$, is normalized so that the double summation of the squared field is equal to one. The variable ω_o is the beam waist, which is described next.

Beam waist is a characteristic that is essential in describing a Gaussian beam. The beam waist, represented by ω_o in Equation (2.3), describes the size of the cross section of the Gaussian beam at the aperture of the laser beam cavity. Knowledge of the beam waist allows for the calculation of the beam width at the target by [9]

$$\omega(z) = \omega_o \sqrt{1 + \left(\frac{\lambda z}{\pi\omega_o^2}\right)^2}, \quad (2.4)$$

where z represents the distance propagated and $w(z)$ is the beam size at range z . The equation explains the inverse relationship between the beam waist at the source and the beam size at the target. The standard deviation of the Gaussian beam at the target is found by dividing the beam size by the square root of two.

2.1.2 Light Propagation. Light propagation and its characteristics are described with many models. A simplified model where light is represented with rays can be explained with geometric optics. More realistic models describe light as waves. These models include diffraction effects, which explain the behavior of light that can't be attributed to reflection or refraction. Two foundational models that explain light diffraction are the Fresnel-Kirchhoff and the Rayleigh-Sommerfeld equations.

The two models are based on the Helmholtz equation [15]

$$(\nabla^2 + k^2) U(x, y, z) = 0, \quad (2.5)$$

where U describes the amplitude and phase of the wave at each point in space and $k = 2\pi/\lambda$, is the optical wave number. The variable λ represents the wavelength of light. The variable ∇^2 is the Laplacian which describes the propagation of electromagnetic waves in the form of paraboloidal waves [14]. The Helmholtz equation treats light as a scalar phenomenon, neglecting the vector characteristics given by Maxwell's equations for electromagnetic fields [16]. The complex field U is calculated using Green's theorem [16]

$$U(x, y) = \iint G_{green}(x - x', y - y') V(x', y') dx' dy'. \quad (2.6)$$

The variables U and G_{green} represent two complex-valued functions of position and V represents a driving function. The function G_{green} is known as Green's function and is dependent on the assumptions made about the problem. In light propagation, Green's function is used to model the path through which light traverses. In optics, this is known as an optical system's point spread function. The architects of the two diffraction models made certain assumptions about the boundary conditions of the aperture, which led to slightly different implementations of Green's function. This led to the two different diffraction models that are described in detail below. In this study's case, the driving function is the field distribution description of a Gaussian beam.

The Fresnel-Kirchhoff diffraction equation is derived by assuming boundary conditions that simplify the equation. The diffraction formula is appropriate as long as two assumptions are met. The two assumptions state that the diffracting aperture must be large compared with the wavelength of light and the diffracting fields must not be observed close to the aperture, meaning that the observation distance is much greater than the wavelength of light. For LADAR applications concerning this thesis,

both conditions are easily satisfied. Despite making assumptions about the boundary conditions of the complex fields, experiments have shown that the model accurately predicts the behavior of electromagnetic fields as long as the two assumptions mentioned earlier are met [16].

Although the Fresnel-Kirchhoff diffraction model fairs well in describing diffracting light, the Rayleigh-Sommerfeld diffraction model performs better in a wider range of applications due to the lower number of assumptions made while considering boundary conditions of the aperture [15]. The following Rayleigh-Sommerfeld diffraction model is shown by [16]

$$U(x, y, z) = \frac{-i}{\lambda} \int_{x'} \int_{y'} U_0(x', y', 0) \frac{z}{l^2} e^{(ikl)} dx' dy', \quad (2.7)$$

where $k = 2\pi/\lambda$, z is the propagation distance from the source to target, and the l represents the total distance between various points in the source and field plane and is calculated with $l = \sqrt{(x' - x)^2 + (y' - y)^2 + z^2}$. The equation accurately models the behavior of light that emerges from a small source and propagates to the far field. The Rayleigh-Sommerfeld diffraction model is incorporated into the LADAR model to propagate the light from the source to the target.

2.1.3 Laser Beam Target Interaction. As the previous sections in this chapter have demonstrated, determining the amount of light that illuminates a target down range is straightforward. However, seeking the light intensity reflected back onto the LADAR detector is a problem that involves many factors. First, the potential light interactions with the target are explained as well as the justifications for the simplification process. Then, the calculation of the intensity of the reflected light incident upon the detector is broken down in Section 2.1.6.

The process of understanding the reflection of light incident off a random object involves many complicated parameters and statistical analysis to truly define the interaction. The laser radar target-signature phenomena includes polarization effects, an-

gular characteristics, spatial characteristics, range characteristics, and Doppler characteristics [17]. These phenomena are explained as well as the different approaches taken to mathematically characterize their influence on the amount of light reflected back at a LADAR detector.

The polarization of light describes the direction of motion of light relative to its motion in the longitude direction. When light interacts with an object, the polarization state of the light has the potential to change. The change in polarization is dependent on several factors. First, the change in the polarization of light illuminating a target is highly dependent on the target shape [17]. Secondly, the polarization of light is dependent on the coherency and specular reflection from the target. For this study, the targets are assumed to have a rough surface relative to the wavelength of light. When the surface is larger than the wavelength of light, diffuse reflections occur [14]. Therefore, it can be assumed that the light reflected back from a target is incoherent, eliminating the concern of polarization effects on the reflected light.

Doppler effects that occur on the incident light include frequency shifting and Doppler spread. This phenomenon is caused by the movement of the target or sensor during the sensing process [17]. For a pulsed laser, frequency shifting will have no effect on the pulse width of the beam. Also, the sensor and target are assumed to be stationary in the simulation; therefore, Doppler effects are not taken into account in this study.

The angle resolved *bidirectional reflection distribution function* (BRDF) is a four dimensional function that describes how light is reflected off surfaces. The BRDF ignores Doppler and polarization effects and considers both the specular and diffuse reflections of light. The BRDF is a ratio of the average reflected radiance to the incident irradiance as a function of the propagation directions of incidence and reflection [17]. A generalized BRDF that only includes illumination and viewing angles is

described by [8], [18],

$$BRDF = BRDF_{spec} + BRDF_{diff} = \frac{A}{\cos^6(\theta)} \exp\left(\frac{-\tan^2(\theta)}{s^2}\right) + B\cos^m(\theta), \quad (2.8)$$

where A and B are constants that describe the ratio of specular and diffuse behavior, θ is the incident angle relative to the normal, s is the surface slope, and m is a parameter describing the diffuse surface.

The target interaction is further simplified by making an assumption about the orientation of the LADAR relative to the target and the target's surface. If the LADAR system is normal relative to the target plane, then the cosine functions become one. Also, if the target is considered rough, an assumption stated earlier to mitigate polarization effects, then specular reflection can be ignored. Given the assumptions listed above, the BRDF becomes a constant that only addresses diffuse reflections. Though the BRDF was marginalized, additional characteristics of the light target interaction are defined in Sections 2.1.4 and 2.1.5.

2.1.4 Pulse Width Expansion. Pulse width expansion or pulse broadening describes the widening of a laser pulse in the temporal domain due to an extended reflection off a target's surface. In an ideal setting, a LADAR pulse strikes a target with a completely flat surface with normal incidence, and the light reflection is modeled with a single impulse. In this case, the reflected pulse's temporal profile and transmitted pulse are identical. If the target has a sloped surface relative to the pulse incident angle, multiple impulses are possible. In this case, the reflected pulse's temporal profile can be wider than the transmitted pulse, depending on the length of the continuous return and the temporal sampling rate. The pulse width expansion calculation is incorporated into [11]

$$P_{tot}(m, n, t_k) = \sum_{kk=1}^{N_s} P_{det}(m, n, t_k - t_{kk}) T_p(m, n, t_{kk}), \quad (2.9)$$

where P_{det} represents the power detected from the reflected light off of the target and T_p represents the target profile. The variable P_{det} is discussed in detail in Section 2.1.6 and the implementation of T_p is discussed in Chapter III. The variables m and n are the indexed locations for each pixel in the detector array. The main takeaway from Equation (2.9) is the pulse width expansion of the Gaussian pulse is modeled using a convolution of the range equation and multiple delta functions calculated into the target profile.

2.1.5 Target Dependent Characteristics. A further description of light's reflection behavior is needed to fully capture the light target interaction. External light reflections off a target are summed up by the two categories of specular and diffuse reflection. Specular reflection occurs when light is incident upon a smooth surface and the light that is remitted by the surface atoms combines to form a single well-defined beam. Diffuse reflection occurs when light is incident upon a rough surface and the light that is reemitted by the surface atoms is scattered in all directions independent of the light incident angle [14]. As mentioned in Section 2.1.3, specular reflections are ignored in this study.

When diffuse reflections occur, the reflected radiation is spread out over an angle that is larger than the incident angle. To an observer or sensor, the light reflecting off an object is the same regardless of the angle of observance. This diffuse reflection is commonly described as a Lambertian reflection. Due to the wide angle of observance, the power of the light reflected off the target is proportionally reduced by the Lambertian reflection shown by [11]

$$P_{ref}(m, n, k) = \frac{\tau_a \rho_t P_t(m, n, k)}{\theta_R(dA)}, \quad (2.10)$$

where θ_R is the solid angle over which radiation is dispersed, P_{ref} is the intensity of light reflected off the target in W/m^2 , τ_a is the atmospheric attenuation and is described in Section 2.1.6, and ρ_t is the reflectivity coefficient. For a Lambertian reflection, the angle over which the radiation is dispersed is π . The variable dA

accounts for the observed area of each pixel at the distant plane where the target is located. The variables m and n are indexed locations for the pixel FOVs at the target plane. The reflectivity coefficient is explained further below.

The reflective nature of the target must be considered when determining the light interaction with the target. The reflective characteristic of a surface describes the ability of a material to reflect radiation [11]. For mirror like materials that typically display specular reflection characteristics, the reflectivity coefficient value can range from 1 to 0.25. Materials that display a diffuse reflection have reflectivity coefficient values ranging from 0.25 to 0.02 [11]. The LADAR simulation developed in Chapter III uses a reflectivity coefficient of 0.25, within the range attributed to diffuse reflections.

2.1.6 Range Equation. The range equation is used to calculate the power of light incident upon the LADAR detector and is shown [11]

$$P_{det}(m, n, k) = \frac{D_R^2 \pi (dA) P_{ref}(m, n, k) \tau_o \tau_a}{4R^2}, \quad (2.11)$$

with P_{det} that represents the power detected at the receiver as a function of position and discrete moments in time. The range equation contains variables that are dependent on the propagation path, target, and LADAR equipment. In this equation, m and n are the spatial coordinates of pixels in an array and k marks the discrete time samples. The variable P_{ref} is the power of the laser pulse reflected off the target area, which is calculated by Equation (2.10). The signal generated from the reflected pulse is compared to a timing function to determine the range to the target surface for each pixel. The rest of the variables in Equation (2.11) are defined below.

The propagation path variable related to Equations (2.10) and (2.11) is τ_a , the atmospheric transmission loss. The variable accounts for the attenuation of the signal due to the absorption and scattering from atmospheric molecules, dust particles, and aerosols. The attenuation factor is highly dependent on wavelength. Experimental results comparing lasers with wavelengths of 2 and 10 microns have shown

that smaller wavelengths are less susceptible to atmospheric attenuation than larger wavelengths [19]. The LADAR simulation developed in Chapter III uses a laser with a wavelength of 1.55 microns, therefore, the atmospheric transmission loss value is set at one. A value of one for the atmospheric transmission loss value indicates that there is no loss of light due to the atmosphere.

The target dependent variables in Equation (2.11) are ρ_t , θ_R , and possibly dA . The first two variables are used to determine P_{ref} and are described in detail in Section 2.1.5. The surface area variable, represented by dA , is dependent on the detector field of view, the laser beam size at the target, and the target size. The variable dA is the smallest area presented when the three surface areas are compared. Due to the design of the LADAR system detailed in Chapter III, the dA parameter is dictated by the detector's field of view. More specifically, since Equation (2.11) is defined for each pixel in the detector array, dA represents the *Field of View* (FOV) of each pixel.

The variables dependent on the LADAR equipment in Equation (2.11) are τ_o and D_R . The area of the receiver aperture constrains the amount of power received at the LADAR detector. The area of the aperture is dictated by the variable D_R , which represents the diameter of the receiver lens, seen in Equation (2.11). The variable τ_o represents the efficiency at which the detector captures light from the receiving aperture. The transmission efficiency of the LADAR equipment is fairly high unless the light incident upon the LADAR aperture is shared among a group of sensors [11]. Since this is not the case for this study, the value of τ_o is set to one.

2.1.7 Noise Modeling. There are multiple sources of noise that interfere with detecting LADAR signal returns. Multiple noise sources originate from electrical components of a detector, background light illuminating a target scene, and speckle noise introduced by the laser reflection itself. The noise components and their statistical distributions are explained in this section.

Photon counting noise is involved with the signal because of the direct detecting *avalanche photo diode* (APD) incorporated in most LADAR systems. The noise source is best described by the following quote, “The number of photon-electrons counted during time δt is a random variable whose mean is proportional to the expected number of photons” [11]. For single mode laser radiation, the photon counts follow Poisson statistics [20]. The photon counting noise is incorporated into Equation (2.12).

Laser speckle is a characteristic of reflected light off rough-surfaces that produce diffuse reflections [17]. The most significant characteristic of light that affects laser speckle is its coherency. Coherency refers to the ability of a light beam to interfere with a version of itself [20]. The coherency of light along with the expected value of the photon count measurements permit the defining of the variance of speckle noise

$$\sigma_{speckle}^2 = E[N_{signal}] \left(1 + \frac{E[N_{signal}]}{M} \right). \quad (2.12)$$

A value of one for M represents a very high coherence and for fully incoherent light the value of M approaches infinity. To generate random noise, the variance of the speckle noise applied to the negative binomial distribution is utilized to produce an accurate representation of speckle and photon counting noise in a signal [11]. Background noise is considered shot noise that is received by the detector that didn’t originate from the laser transmitter [11]. Most background noise is attributed to the sun illuminating the target. Since the random arrival of photons generated from background light that are received by the detector can’t be used for ranging, they are considered noise. Photons that are incident on an APD detector are generated using a Poisson distribution [21], and the calculation for the mean of the Poisson distribution for background noise is given by [11]

$$E[N_b] = \frac{S_{IB} \Delta_\lambda dA \rho_t \eta \tau_a \tau_o D_R^2 \Delta t \lambda}{4R^2 h c} + E[N_{dark}]. \quad (2.13)$$

The variables dA , τ_o , τ_a , and D_R are covered in Section 2.1.6. The variable ρ_t is the reflectivity coefficient and is described in Section 2.1.5. The variable R is the

range to target and the variable h is Planck's constant. The variables λ and c refer to the wavelength and speed of the light. The amount of noise generated is based partially on Δ_t , the sampling rate in time. The variable S_{IB} is the intensity of the background light at the target measured in units of W/m^2 per μm of electromagnetic bandwidth. The variable Δ_λ is the electromagnetic bandwidth in μm of an optical bandpass filter present in the LADAR system. The calculation also includes dark current, represented by N_{dark} , which is defined as a small current that flows through an APD when there are no photons incident upon the detector.

The thermal radiation is classified as electromagnetic energy (photons) that is emitted by all objects [14]. The distribution of thermal radiation is considered Gaussian in nature [22]. The variance of thermal noise is shown by [11]

$$Q_n^2 = \frac{k_b TC}{q_e^2}, \quad (2.14)$$

where Q_n^2 is the charge variance of thermal electrons. The other parameters influencing thermal noise are Boltzmann's constant (k_b), the temperature of the circuit (T), the capacitance of the circuit (C), and the charge of an electron (q_e).

2.1.8 Detector Characteristics. A detector is a device that converts incident photons into electrical signals. APDs are commonly used as detectors for direct-detection LADAR systems. In addition to detecting incident photons, the APD can also amplify the signal. The ability of the APD to amplify the signal is used to adjust the *signal to noise ratio* (SNR) by [11]

$$SNR_{APD} = \frac{G_{apd} N_{signal}}{\sqrt{Q_n^2 + G_{apd}^2 \sigma_{speckle}^2 + G_{apd}^2 N_b}}, \quad (2.15)$$

where G_{apd} is the gain parameter of the APD. The gain limit setting of an APD is dependent on the manufacturer, as some can provide gain ranging from one to orders of 1000. But, the effectiveness of the gain setting in an APD is limited by speckle and background noise.

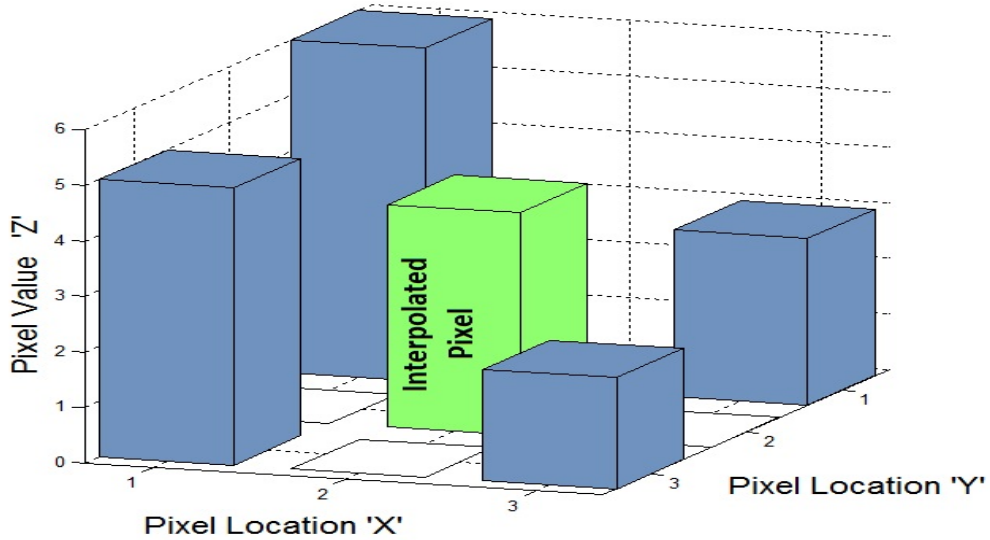


Figure 2.4: Three dimensional interpolation of one pixel. The pixel value represents the height of an object in this study.

2.2 Interpolation

Interpolation is the process of inserting data points that are calculated with an algorithm between observed data points. This study seeks to increase the resolution of a LADAR produced image by utilizing interpolators to insert more points in the point cloud. Effective interpolation is desired to reduce the data rate of the LADAR equipment while not compromising on the quality of the images.

There are many techniques that are used to accomplish interpolation. In this study, we use four different interpolators: sinc, spline, linear, and Hermite. The first three interpolators use information from the range estimations. The Hermite interpolator uses information from the range and pulse width expansion estimations. The interpolators are first described in *two dimensional* (2D) space. Then, each interpolator's implementation in 3D is briefly discussed.

2.2.1 Linear Interpolation. Linear interpolation is a simple technique to quickly insert additional points between the actual observed data points. This tech-

nique is often used to fill in points in a table. The interpolator is described by [4]

$$y = y_0 + (x - x_0) \frac{(y_1 - y_0)}{(x_1 - x_0)}, \quad (2.16)$$

where x_0 , y_0 , x_1 , and y_1 are the observed values and y is the interpolated value at inserted position x . Linear interpolation produces adequate results, but the ability to approximate values is limited to the distance between the two observed points.

Bilinear interpolation is often used in computer image processing [23]. Bilinear interpolation is executed similarly to linear interpolation, with the exception being the number of observation points considered. Bilinear interpolation averages the values of four observation points, and places that averaged value equidistant between the four observation points, shown in Figure 2.4. This study implements bilinear interpolation by incorporating a built in software function.

2.2.2 Sinc Interpolation. Sinc interpolation is used for signal reconstruction to oversample an observed signal in an effort to smooth out the signal [6]. The sinc interpolator is implemented in the same manner as a low pass filter on a signal. The sinc interpolation function is defined as [6]

$$f_{sinc}(x) = \sum_n f_{samp}(nT) \text{sinc} \left[\frac{\pi}{T} (x - nT) \right], \quad (2.17)$$

where T is the sampling period, n is the over sampling rate of the sinc function, and $f_{samp}(nT)$ is the sampled function. For interpolation, the variable x in Equation (2.17) represents the observations of the original signal.

The implementation of the sinc interpolator on a 3D image requires a 2D sinc filter. The 2D sinc filter is defined as

$$\text{sinc2}(x, y) = \text{sinc}(x) \text{sinc}(y), \quad (2.18)$$

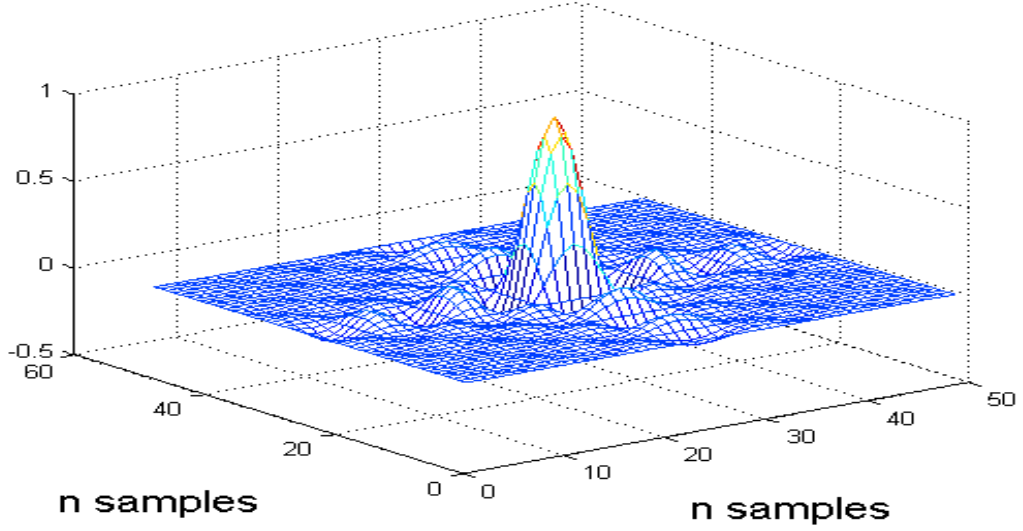


Figure 2.5: The 2D sinc filter. The sampling interval for the sinc filter is $1/4$.

which is shown in Figure 2.5. The filter is convolved with an undersampled image for 2D sinc interpolation. This study spatially down samples images by a factor of two and four for purpose of subsequent interpolator evaluation. The sampling period is $\pm 2\pi$ and the sample interval is the inverse of the down sampling factor.

2.2.3 Spline Interpolation. Spline interpolation is often applied in the computer graphics industry because of its simplicity and ability to model complex curves and surfaces. Specifically, spline curves are used in image processing for magnification and noise smoothing [24]. This study incorporates a cubic spline function detailed by [5], [24]

$$f_{spline}(x) = a_i + b_i(x - x_i) + c_i(x - x_i)^2 + d_i(x - x_i)^3, \quad (2.19)$$

where $x_i \leq x \leq x_{i+1}$, and $f_{spline}(x)$ is the oversampled function that travels through the observed data points. The coefficients of Equation (2.19) are dependent on the observed samples of the data. The 2D spline interpolation technique is applied to the down sampled images using built in functions in software.

2.2.4 Hermite Interpolation. Like the interpolators described formerly, the Hermite interpolator uses observed data points to approximate additional points in between the measured set of points. In addition, the Hermite interpolator also considers the slope of the measured data points. Consider the function $f(x)$ with derivative $f'(x)$, for which value and slope data are available on a grid of points: $f_i = f(x_i)$ and $f'_i = f'(x_i)$ for $i = 1, \dots, N_x$. An approximating function is desired within the point cloud of observation points. The function is defined piecewise using a cubic ordered Hermite interpolator. The construction of the functions begins with normalizing the subinterval between the two observation points x_i and x_{i+1} with $u(x) = (x - x_i)/(x_{i+1} - x_i)$. Due to normalization, the coefficients of the cubic Hermite function are calculated on the interval $[0, 1]$, assuming the tangent of the first point is zero and for the second point is one. The local basis polynomials are [5]

$$\alpha(u) = 1 - 3(u)^2 + 2(u)^3, \quad (2.20)$$

$$\beta(u) = 1u - 2u^2 + 1u^3, \quad (2.21)$$

where $\alpha(u)$ is the basis polynomial for the range estimations and $\beta(u)$ is the basis polynomial for the surface slope estimations. The Hermite cubic interpolating function is defined as

$$p_i(u) = f_i\alpha(u) + f'_i\Delta x_i\beta(u) + f_{i+1}\alpha(1-u) - f'_{i+1}\Delta x_i\beta(1-u), \quad (2.22)$$

with $\Delta x_i = x_{i+1} - x_i = dx/du$ accounting for the change in variable and $p_i(u)$ is the interpolating polynomial.

The advantage of including the gradient information into the Hermite interpolator is shown in Figure 2.6. The Hermite interpolator clearly follows the truth data closer than the cubic spline interpolator. The *root mean square error* (RMSE) calculation confirms what is seen visually in Figure 2.6. The RMSE calculation of the spline interpolator is 0.22, compared to a RMSE value of 0.14 for the Hermite

interpolator, shows a 36% improvement. In addition, if the linear interpolator was shown, it would clearly miss the peaks of the truth data based on the observations taken from the truth data.

For three dimensions, the bi-Hermite interpolation function with grid cell defined as $(x_i \leq x \leq x_{i+1}, y_j \leq y \leq y_{j+1})$, is shown by

$$\begin{aligned}
p_{i,j}(u(x), v(y)) = & \sum_{\Delta i=0}^1 \sum_{\Delta j=0}^1 (f_{i+\Delta i, j+\Delta j}) \alpha_{\Delta i}(u) \alpha_{\Delta j}(v) \\
& + \sum_{\Delta i=0}^1 \sum_{\Delta j=0}^1 \Delta x_i \left(\frac{\partial f}{\partial x} \right)_{i+\Delta i, j+\Delta j} \beta_{\Delta i}(u) \alpha_{\Delta j}(v) \\
& + \sum_{\Delta i=0}^1 \sum_{\Delta j=0}^1 \Delta y_j \left(\frac{\partial f}{\partial y} \right)_{i+\Delta i, j+\Delta j} \alpha_{\Delta i}(u) \beta_{\Delta j}(v), \tag{2.23}
\end{aligned}$$

with $\alpha_0(u) = \alpha(u)$, $\alpha_1(u) = \alpha(1-u)$, $\beta_0(u) = \beta(u)$, $\beta_1(u) = -\beta(1-u)$, and similarly for $v(y) = (y - y_j)/(y_{j+1} - y_j)$. The resulting interpolation is piecewise-defined over the grid but is continuous in value and in both first partial derivatives everywhere within $[x_1, x_{Nx}] \times [y_1, y_{Ny}]$. The variable $p_{i,j}$ is the interpolating polynomial for the 3D Hermite algorithm.

2.3 Sampling

The digitization of the continuous signals represented in the LADAR system introduces sampling constraints that need to be addressed. The 3D image dictates the domains in which the sampling constraints occur, the time and spatial domains. The sampling constraints are defined by the Nyquist sampling theorem, which states that the sampling frequency has to be greater than twice the bandwidth of the signal to avoid aliasing [3]. The Nyquist sampling rate is desired to set the limits of sampling tolerance before the integrity of the images are lost. The sampling constraints of the LADAR system model are investigated for both domains.

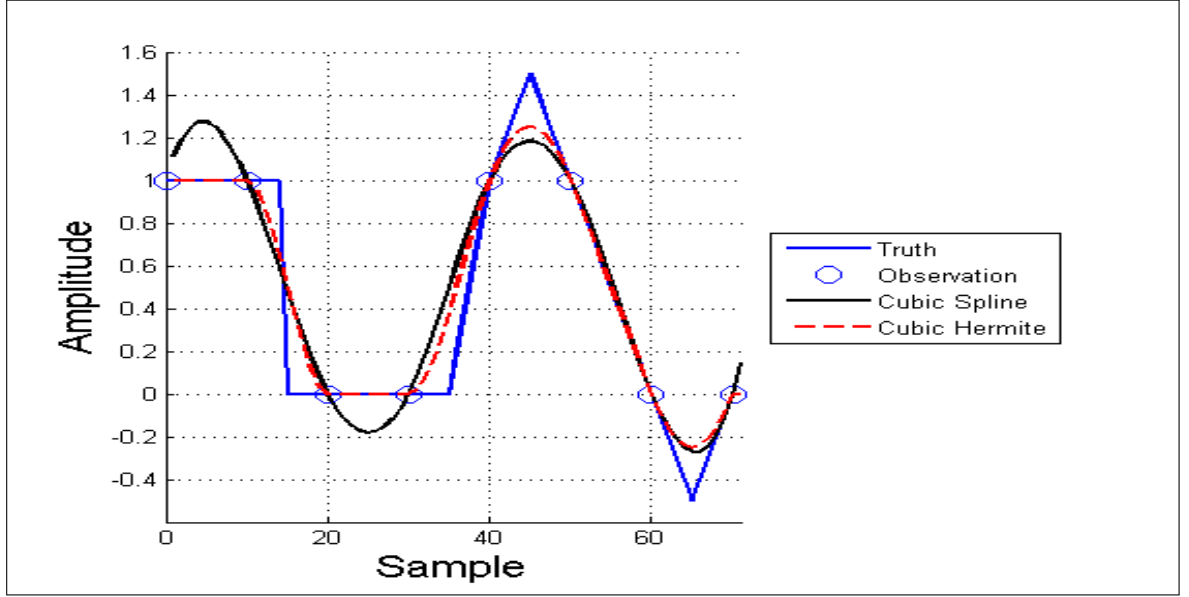


Figure 2.6: The two dimensional interpolation comparison between the cubic spline and cubic Hermite.

2.3.1 Time Domain Sampling Constraint. To gain insight into the temporal sampling constraint dictated by a Gaussian pulse, it is analyzed in the frequency domain. The Fourier transform of a Gaussian equation is shown [11]

$$\int_{-\infty}^{\infty} \frac{E_t}{\sigma_w \sqrt{2\pi}} \exp \left[\frac{-t^2}{2\sigma_w^2} \right] \exp [-j2\pi ft] dt = E_t \exp \left[\frac{-f^2}{2 \left(\frac{1}{4\sigma_w^2 \pi^2} \right)} \right]. \quad (2.24)$$

The standard deviation of the generalized Gaussian function in the frequency domain is shown

$$\sigma_f = \frac{1}{2\sigma_w \pi}. \quad (2.25)$$

Assuming that the cut off frequency of a Gaussian function is set at $\pm\pi$ standard deviations away from the mean for minimal aliasing, it is defined as [11]

$$f_c = \frac{1}{2\pi\sigma_w} \cdot \pi \rightarrow f_c = \frac{1}{2\sigma_w}. \quad (2.26)$$

Twice the cutoff frequency is the Nyquist sampling rate in the frequency domain. The time domain sampling requirement is determined by the Nyquist sampling frequency

shown

$$f_n = 2f_c = \frac{1}{\sigma_w} \Rightarrow \Delta t = \sigma_w, \quad (2.27)$$

where f_n is the sample rate in the frequency domain and Δt is the sampling rate in the time domain. Therefore, the minimum sampling rate in the time domain based on the Nyquist criterion is the standard deviation of the Gaussian pulse implemented in the time domain.

2.3.2 Spatial Domain Sampling Constraints. The time sampling constraints are driven by the target properties and the Gaussian pulse's profile in the time domain. The temporal profile of the Gaussian pulse is investigated to find the requirements for sampling in the temporal domain. The spatial sampling constraint is initially established by investigating the sampling rate of a Gaussian beam. Once the Gaussian beam's sampling constraint in the target plane is established, the target's involvement in the system's spatial sampling constraint is discussed.

A Gaussian beam's minimum sample size in the receiver plane is determined by [11]

$$\Delta_{GB} < \frac{\lambda z}{6\sigma_w}, \quad (2.28)$$

where σ_w is the beam waist of the Gaussian pulse at the transmitter, λ is the wavelength of the light, and z is the target distance. In this instance, the receiver plane is classified as the target plane. As discussed in Section 2.3.1, the sampling limit utilized in Equation (2.28) assumed the standard deviation is established as the minimum sampling size for a Gaussian function. The sampling limit is determined in only one dimension due to the symmetry of the Gaussian beam.

The Gaussian beam has set the sampling constraint limit in the target domain. This sampling rate can be further limited by the target shapes. There are four different targets used in the simulation that are introduced in the Chapter III. The Nyquist sampling rate in the spatial domain is investigated for the target shapes in

Section 3.1.1 to find the overall spatial sampling limitation in the target plane for the LADAR simulation.

2.4 Estimation Theory

This study requires estimations for the range of each pixel as well as the pulse width expansion of each detected pulse. Several authors have investigated the merits of different pulse detection methods. Peak, constant fraction (also referred to as 50% leading edge), and matched filter (also called correlation detection) detection methods are frequently compared against simulated incoherent and coherent LADAR signals [13], [18], [25], [26]. The matched filter outperformed the other detection methods on a consistent basis over a wide range of conditions. Therefore, the correlation detection method is utilized to estimate the range and pulse width expansion of each pulse in this study. The Pearson's Product-moment coefficient, described by [27]

$$\rho = \frac{1}{N} \sum_{n=1}^N \frac{(d_n - \bar{d})(r_n - \bar{r})}{\sigma_d \sigma_r}, \quad (2.29)$$

is used to compare reference waveforms with the data received. Here, \bar{d} and \bar{r} represent the mean value for the data and reference waveforms. The variables σ_d and σ_r represent the standard deviation of the data and reference waveforms. The correlation coefficient, ρ , takes on the value between one and negative one indicating the linear association between the two waveforms [27]. The estimation process favors the correlation coefficient values that have the greatest value.

The range and pulse width expansion are accurately determined by comparing reference waveforms with the received reflected LADAR beam. Reference waveforms for the range estimation are generated by using a window of ranges with Equation (2.1). These waveforms are compared with the received pulse and an estimated range per pixel is established. The pulse width is therefore estimated by comparing the data received against an array of reference waveforms generated using a 2D form

of Equation (2.9). Once the pulse width expansion is estimated, the magnitude of the slope of the surface of the target that is in the FOV of each pixel is calculated.

2.5 Chapter Summary

This chapter discussed the background material needed in several key subjects. The development of the LADAR model required merging several areas of optical science together to build an accurate model. The development began with the formulation of the light pulse and then proceeded to a discussion about the reasoning and selection of the propagation function for the light. The light and target interaction were covered in Sections 2.1.3 through 2.1.5 considering the involved physical interactions and then the simplification of those interactions. The detection of the reflected pulse at the LADAR detector was scrutinized in Sections 2.1.6 and 2.1.8. Noise sources that are involved with LADAR signals were discussed as well as their statistical distributions in Section 2.1.7. The general estimation algorithms for LADAR signals were covered in Section 2.4. The interpolation techniques that are applied against the LADAR returns in Chapter III are explained in Section 2.2.

The next chapter, Chapter III, discusses the execution of the LADAR model and the different parameters that are tested. A description of the estimation and interpolation processes on the simulated LADAR data are also covered.

III. Research Methodology

The research methodology begins with introducing and describing in detail the implementation of the LADAR model. The LADAR model is constructed in parts to simplify the explanation. In addition to the model, the execution of the estimation and interpolation processes are described. Once the foundational processes are explained and defined, the testing procedures and reasoning are disclosed.

3.1 *Parameters of LADAR Model*

To construct a consistent model, the operating parameters need to be defined. The conditions for the LADAR system are consistent with models covered during the literature review process [11], [18]. The LADAR system constraints also reflect the assumptions made concerning the development aspects of the LADAR model. The parameters that remain consistent throughout the model and testing procedures are shown in Table 3.1. There are other system settings that are needed to help define the LADAR model which are varied through the testing process. These variables are listed in Table 3.2.

The purpose for the simulations in this study is to compare the performance of the bi-Hermite interpolator that takes advantage of the pulse width expansion information against three other interpolators that only use range estimations. This study also seeks to find the conditions in which the Hermite interpolator optimally performs. The LADAR model conditions that are varied for testing purposes are the range to target, FWHM of the Gaussian pulse, the sampling rate in time, and the sampling rate in space. Some parameters are dependent on these variable conditions, therefore, they are also variable. All variable settings in the LADAR system are listed in Table 3.2. The logic behind the values listed in the table are explained below. The range to target values and how the LADAR model adjusts due to the dynamic propagation distance are explained in Section 3.5.5.

Table 3.1: Constant system specifications of the LADAR.

Variable	Value	Units	Description
λ	1.55×10^{-6}	Meters	The wavelength of light lazed on target.
ω_o	0.002	Meters	Beam waist size of the Gaussian beam at the source.
τ_a	1	Unitless	The atmospheric transmission loss reflects the attenuation of the light due to the atmosphere. For more details, refer to Section 2.1.6.
τ_o	1	Unitless	The optics transmission loss reflects the attenuation of the light due to the optical lens in the LADAR camera.
θ_r	π	Radians	The diffuse reflection angle.
D_R	0.1	Meters	The lens diameter of the LADAR camera. The variable is used to calculate the area of the aperture.
E	0.05	Joules	Power of the laser in Joules.
ρ_t	0.25	Unitless	The reflectivity coefficient of the target.
r_o	0.05	Meters	The Fried's parameter, sometimes called the seeing parameter.
Detector Size	56 by 56	Pixels	The detector array size of the LADAR. The dimensions of the detector were arbitrarily chosen.
Pixel Size	5×10^{-6}	Meters	The length of a square side of a single pixel.
ν	0.075	Unitless	The quantum efficiency of the detector.
C	1×10^{-12}	Farads	The capacitance of the detector electronics.
T	300	Kelvin	The circuit temperature of the detector.
N_{dark}	1×10^{-9}	Amps	The dark current of the detector circuit.
z_{range}	± 10	Meters	The established range gate dependent on the range to target.
M	90	Degrees	The coherence parameter of the light which represents the degrees of freedom.

Table 3.2: Variable system specifications of the LADAR model.

Variable	Values	Units	Description
Z	10, 9, 8, 7, 6, 5, 4	Kilometers	The distance from the LADAR to the target.
δ_t	0.75, 1.5, 2.25, 3, 3.75, 4.5, 5.25	Nanoseconds	The sampling in time is dependent on the standard deviation of the Gaussian pulse. The sampling in time is established by dividing the standard deviation by the values listed.
τ_g	4, 3, 2, 1	Nanoseconds	The FWHM of the Gaussian pulse generated by the laser cavity.
σ_w	1.70, 1.27, 0.85, 0.42	Nanoseconds	The standard deviation of the Gaussian pulse driven by the values of the variable FWHM.
q	2, 4	Unitless	Spatial down sampling rate. A value of two is classified as <i>low resolution</i> (LR). A value of four is classified as <i>super low resolution</i> (SLR).

The Gaussian pulse model in the time domain, shown by [11]

$$P_t(t) = \frac{E_t}{\sigma_w \sqrt{2\pi}} \exp \left[\frac{-(t)^2}{2\sigma_w^2} \right], \quad (3.1)$$

controls the variables of FWHM, the standard deviation of the Gaussian pulse, and the sampling rate in the time domain. The standard deviation of a Gaussian pulse is calculated using [9]

$$\sigma_w = \frac{\tau_g}{\sqrt{8 \ln(2)}}, \quad (3.2)$$

where τ_g represents the FWHM, whose values are listed in Table 3.2. The standard deviation values that are calculated using Equation (3.2) are listed in Table 3.2. The sampling rate in the temporal domain is derived from the standard deviation of the Gaussian pulse, shown by

$$\Delta t = \frac{\sigma_w}{\delta_t}, \quad (3.3)$$

as discussed previously in Section 2.3.1. The variable δ_t represents the arbitrarily selected values that are based on the Nyquist sampling rate. The range of values for δ_t , listed in Table 3.2, covers a sampling range from slightly under sampled to over five times over sampled. Next, the logic behind the spatial down sampling rates is explained.

3.1.1 Spatial Sampling Constraints. The spatial down sampling rate is dictated by two factors. First, we must know that the current sampling rate by the 56 by 56 detector array is sampling at an acceptable level at the target plane. Secondly, we must have confidence that the down sampled images have enough data for reconstruction by interpolation. As mentioned in Section 2.3.2, the Nyquist sampling criterion will provide the sampling size limit for the target plane. The two factors that are investigated are the illuminating Gaussian beam and the target profiles.

The beam waist of the Gaussian beam is set at 2 *mm*. As mentioned in Section 2.3.2, the Nyquist criterion sampling limit is found using [11]

$$\Delta_{GB} < \frac{\lambda z}{6\sigma_w}, \quad (3.4)$$

for the Gaussian beam down range at the target. The standard deviation of the Gaussian beam at the source is easily found by $\sigma_w = \omega_o/\sqrt{2}$, with a value calculated at 1.41 *mm* [11]. Therefore, the sampling constraint for the Gaussian beam must not be greater than 1.83 meters. With a FOV for each pixel calculated at 0.05 meters down range at 10 *km*, the Gaussian beam happens to be incredibly oversampled. Even considering a spatial down sampling factor of four, each sample occurs at every 0.2 meters, well within the Nyquist criterion sampling constraint.

Now that we know the Gaussian beam is sampled at an appropriate rate, the spatial sampling rate of the target profiles are discussed. Before that can occur, the target profiles need to be introduced. The author utilized four different target profiles, as shown in Figure 3.1. The four profiles have different characteristics and

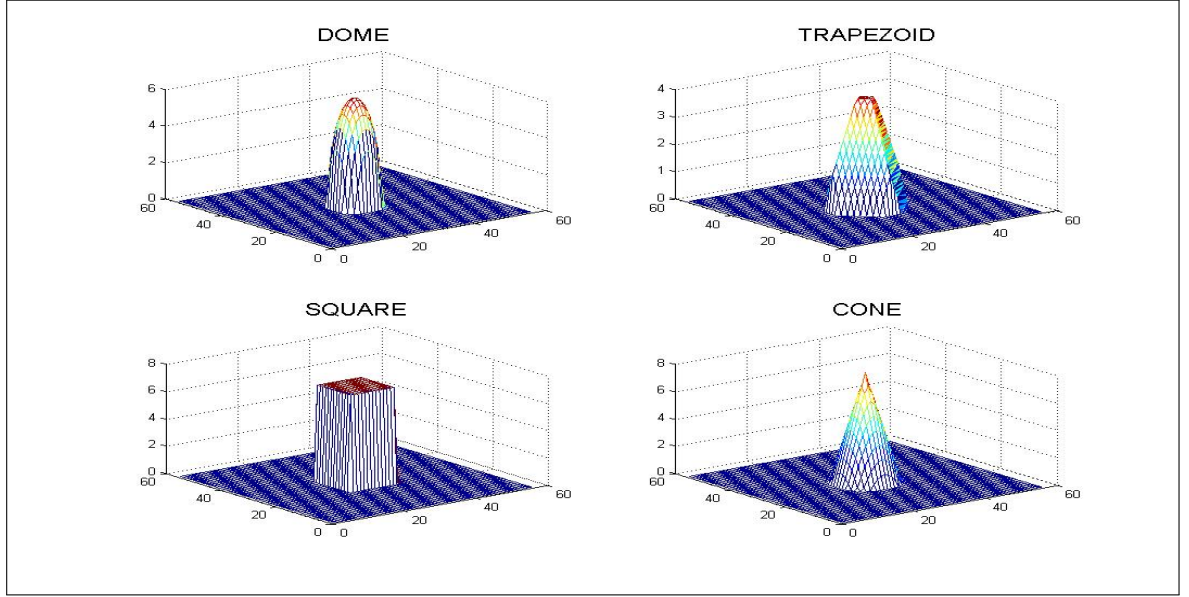


Figure 3.1: Target profiles.

are intended to test the interpolator performance in different ways. The Nyquist spatial sampling limit for the target profiles is approximated by investigating the dome profile. The dome target profile was chosen because it contains both low and high frequency characteristics when compared to the other target profiles.

The dome target profile Nyquist sampling constraint investigation begins with approximating the dome to a Gaussian function. The Gaussian function behavior from the mean ranging out to the first standard deviation compares favorably to the dome shape. Therefore, a 3D Gaussian shape out to one standard deviation with the same diameter size as the dome profile is used to investigate the spatial sampling limit dictated by the targets. The diameter of the dome in the target plane covers 12 pixels, or 0.6 meters. Visually, the approximation occurs by placing a dome inside a standard deviation of the mean of a Gaussian curve. The dome is centered on the mean of the Gaussian curve and its circumference is approximately two standard deviations across. Therefore, a Gaussian shape with a diameter of 1.8 meters, or three times the width of two standard deviations, is desired for an approximation of the dome. Using Equations (2.4) and (3.4), the standard deviation of a Gaussian beam at the source that would expand to the appropriate size down range is 0.85 *mm*.

Now that the standard deviation of the dome sized Gaussian function is known, the sampling constraint of the function is now analyzed.

The Nyquist sampling constraint for a Gaussian function was found to be the standard deviation of the Gaussian, as explained in Section 2.3.1. However, the sampling constraint assumed a cutoff frequency was set at π standard deviations away from the mean. We desire a new cutoff frequency for the Gaussian to be set at one standard deviations away from the mean because of the approximation to the dome shape. The new cutoff frequency is set by

$$f_c = \frac{1}{2\pi\sigma_w} \times 1 \rightarrow f_c = \frac{1}{2\pi\sigma_w}, \quad (3.5)$$

therefore the Nyquist criterion sampling limit is

$$f_n = 2f_c = \frac{1}{\pi\sigma_w} \Rightarrow \Delta d = \pi\sigma_w, \quad (3.6)$$

where Δd represents the minimum spatial sampling rate for a Gaussian beam whose cutoff frequency was established at one standard deviation away from the mean. Now an adaptation to Equation (3.4) is made, shown by

$$\Delta_{DOME} < \frac{\lambda z}{2\pi\sigma_w}, \quad (3.7)$$

which sets the Nyquist driven spatial sampling constraint for the dome, calculated at 0.29 meters. Given that the maximum downsampling period occurs at every 0.2 meters with $q = 4$ shown in Table 3.2, we know that the sampling constraint dictated by the illuminating Gaussian beam and the target profiles are met by the LADAR system.

3.2 3D LADAR Model

3.2.1 Development of 3D Gaussian Beam at Target Plane. The LADAR model begins with the laser beam exiting the laser cavity. The beam waist of the

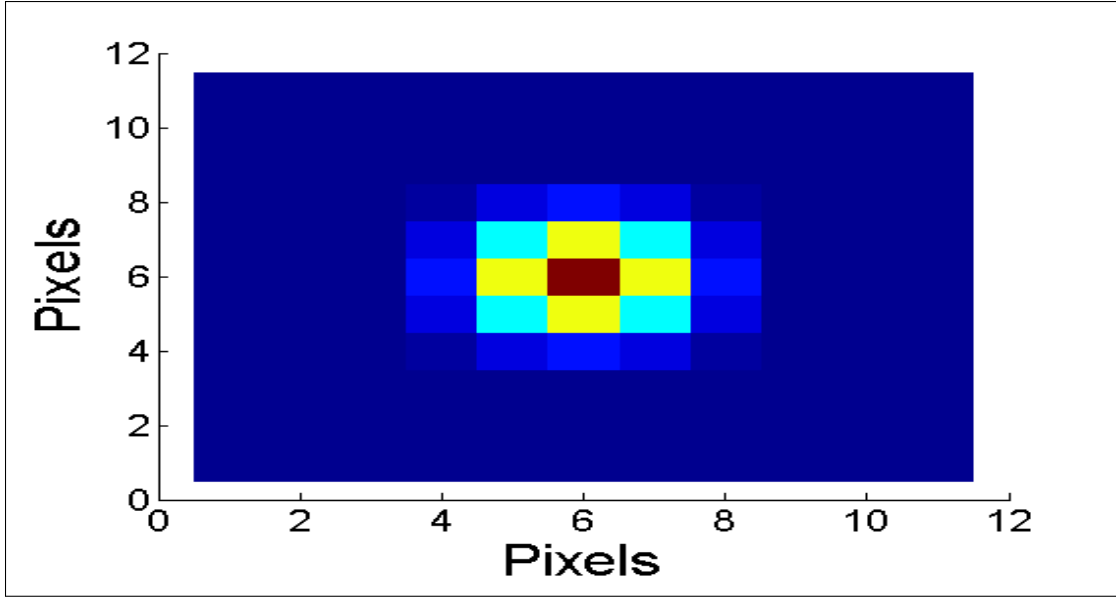


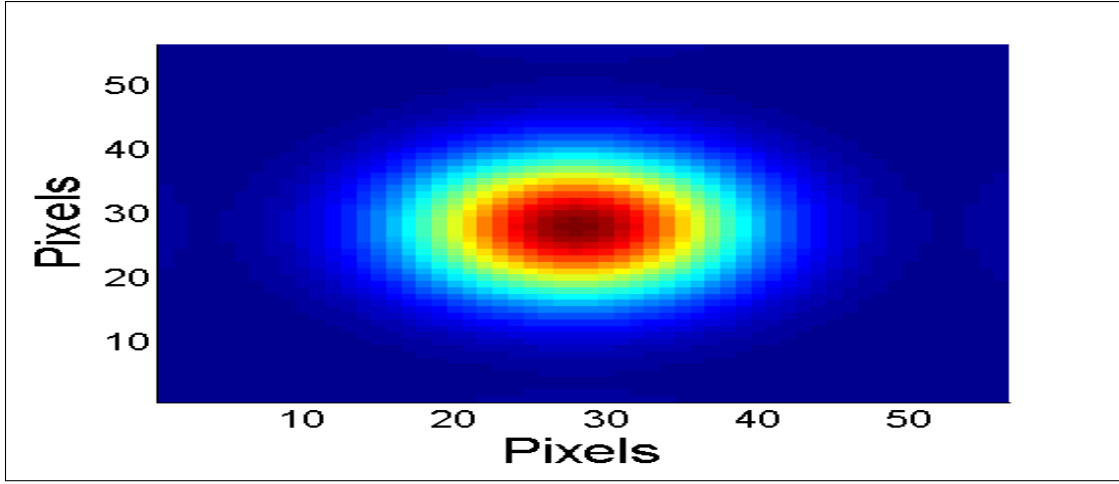
Figure 3.2: The Gaussian beam upon exiting the laser cavity of the LADAR.

Gaussian pulse exiting out of the laser cavity determines the size of the Gaussian beam, given a constant propagation equation. A general 2D Gaussian equation is [11]

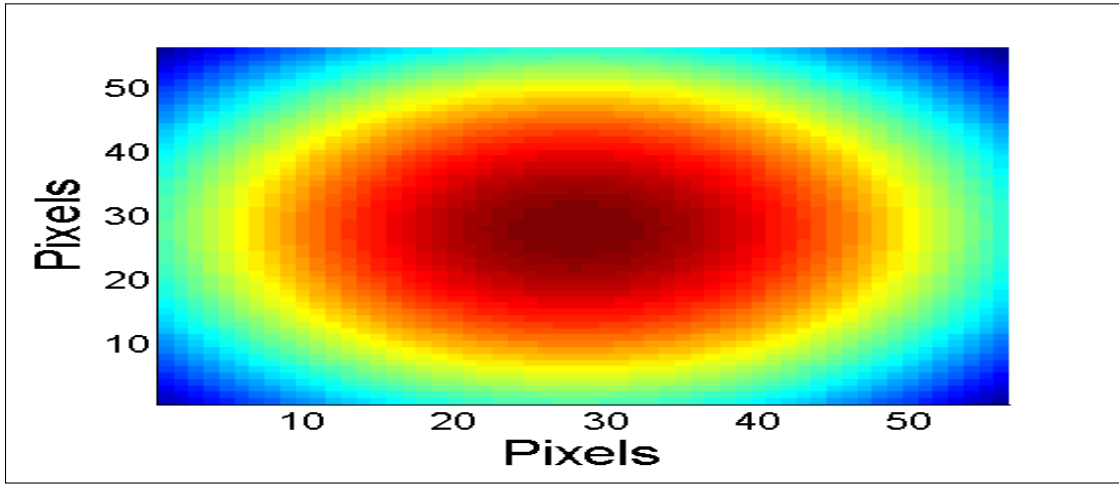
$$g_{lc}(x, y) = \frac{1}{2\pi\sigma_x\sigma_y} \exp \left[\frac{-(x-x_0)^2}{2\sigma_x^2} + \frac{-(y-y_0)^2}{2\sigma_y^2} \right] \quad (3.8)$$

where g_{lc} is the Gaussian beam exiting the laser cavity. The beam is demonstrated in Figure 3.2. The Gaussian beam must now be propagated to the distant plane where the target awaits.

To receive detectable amounts of light at the LADAR, the target needs to be fully illuminated with the transmitted pulse. Ideally, depending on the size of the FOV of the detector, the whole field should be illuminated. In this study's case, illuminating the entire FOV at the target is the goal. The Gaussian beam size needs to completely illuminate the target down range to image the object with LADAR. A general beam waist parameter for a LADAR system imaging objects at several thousand meters was given at 0.009 meters. The two dimensional image of the Gaussian beam with a beam waist of 0.009 meters at the laser cavity is shown in Figure 3.3(a). Through test and evaluation, it was found that a Gaussian beam generated with a beam waist



(a) Beam Waist = 0.009 m



(b) Beam Waist = 0.002 m

Figure 3.3: Two Gaussian beams with different beam waists. The field distributions were created using Equation (3.9) with a propagation distance equal to 10 *km*. The two field distributions contain the same amount of energy (1 Joule). The Gaussian beam with waist of 0.002 meters was selected because it dispersed the energy over a greater area.

of 0.002 meters, shown in Figure 3.3(b), dispersed the power of the beam over a wider area. It was found that the power of the Gaussian beam shown in Figure 3.3(a) was concentrated in the center of the FOV, thus the edges of the image were lost in the noise. The next step in the simulation is to propagate the Gaussian beam shown in Figure 3.2 to the target.

The Rayleigh-Sommerfeld diffraction model was chosen in Section 2.1.2 to propagate the light from a source plane to the distant plane. The Rayleigh-Sommerfeld propagation summation with t held constant is [11]

$$f_{prop}(w_p, s_q) \approx \sum_{m=1}^N \sum_{n=1}^N \frac{g(x_m, y_n) Z \exp [j2\pi (R(x_m, y_n, w_p, s_q)/\lambda)]}{j\lambda R(x_n, y_m, w_p, s_q)^2}, \quad (3.9)$$

where the variables w_p and s_q are the pixel locations for the field in the distant plane and x_m and y_n are the pixel locations in the source plane. The distance between the planes is Z , and the distance between the pixel in the source plane and the pixel in the distant plane is R . The Gaussian beam field distribution in the spatial domain is now established in the target plane. The Gaussian pulse profile in time is incorporated with the Gaussian field distribution by [11]

$$P_t(x, y, t_k) = \frac{E_t(x, y)}{\sqrt{2\pi}\sigma_\omega} \exp \left[\frac{-(t_k - Z/c)^2}{2\sigma_\omega^2} \right], \quad (3.10)$$

creating a 3D Gaussian profile at the target. The field distribution is incorporated into the equation by $E_t(x, y) = E \times f_{prop}(w, s)$, which is the energy distribution of the Gaussian beam at the target plane. The variable representing time, t , is iterated over the entire range gate, given in Table 3.1. The power of the Gaussian beam is the energy field divided by time. Now that the power of the Gaussian beam at the target is described in 3D, the range equation and target profile are utilized to generate the light reflected off the target as seen by the LADAR detector.

3.2.2 Beam Target Interaction. The target interaction is calculated by creating a target profile and convolving it by the range equation. The range equation is [11]

$$P_{det}(m, n, k) = \frac{\tau_o \tau_a^2 D_R^2 P_t(m, n, k)}{R^2 \theta_R}, \quad (3.11)$$

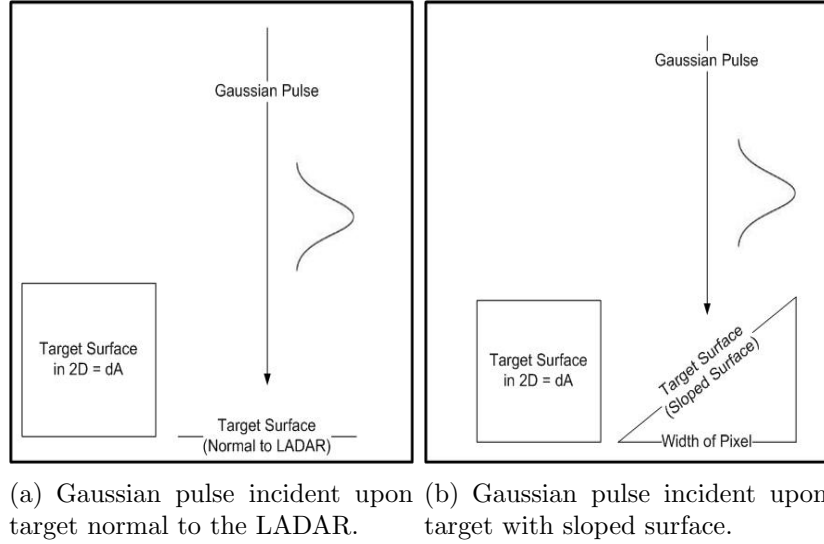


Figure 3.4: Comparison of Gaussian pulse interaction with two different target slopes.

where P_t is the power of the transmitted Gaussian pulse at the target. The variables ρ_t and dA that were in the range equation described by Equation (2.11) were moved to the target profile equation because the parameters are target dependent.

The target profile is calculated based on the characteristics of the target. Each pixel of the image has a set of unique characteristics. For this study, the reflectivity coefficient, explained in detail in Section 2.1.5, is constant over the FOV of the detector array. Therefore, the unique characteristics of each pixel only concern the area and the slope of the target. The area of each pixel is constant because all the pixels in the array are the same size. However, the target profile equation can include multiple returns, depending on the slope of the target. The target profile equation is

$$T_p(m, n, k) = \frac{dA}{n_{returns}} \rho_t \delta(m, n, k), \quad (3.12)$$

where $n_{returns}$ is the total amount of impulse returns based on how long it takes for the Gaussian pulse to propagate through the object's surface. The locations for the impulses, depicted by k , are centered on the location where the target profile surface occurs in the range gate. Each additional impulse is placed in alternating locations of

its nearest neighbor. Locating the impulses in this way produces a widened Gaussian pulse that peaks at the range location of the target surface. The variable δ is the Dirac delta function, with the number of impulses determined by

$$n_{returns} = \left\lceil \frac{x \tan(\theta(m, n))/c}{\Delta t} \right\rceil, \quad (3.13)$$

where x is the width of the pixel in the distant plane, Δt is the sampling period in time, and θ is the angle of the slope of the pixelated target. The numerator represents the length of an unknown side of the triangle in Figure 3.4(b) divided by the speed of light.

The calculation of the power of the laser reflection off the target incident on the LADAR detector is [11]

$$P_{tot}(m, n, t_k) = \sum_{kk=1}^{N_s} P_{det}(m, n, t_k - t_{kk}) T_p(m, n, t_{kk}), \quad (3.14)$$

which is the convolution of the target profile and the range equation. Next, noise is added into the signal to reflect the types of interference that a LADAR system experiences.

3.2.3 Additive Noise. There are three functions that incorporate four different noise sources that are added into the signal. The three functions have different distributions, therefore, they are generated independently and summed into the signal produced by Equation (3.14). Before the noise is added in with incident light, the signal must be converted from watts to photons. The relationship used to convert between watts and photons is [11]

$$N_P = P_{tot} \frac{(\Delta t) \eta \lambda}{hc}, \quad (3.15)$$

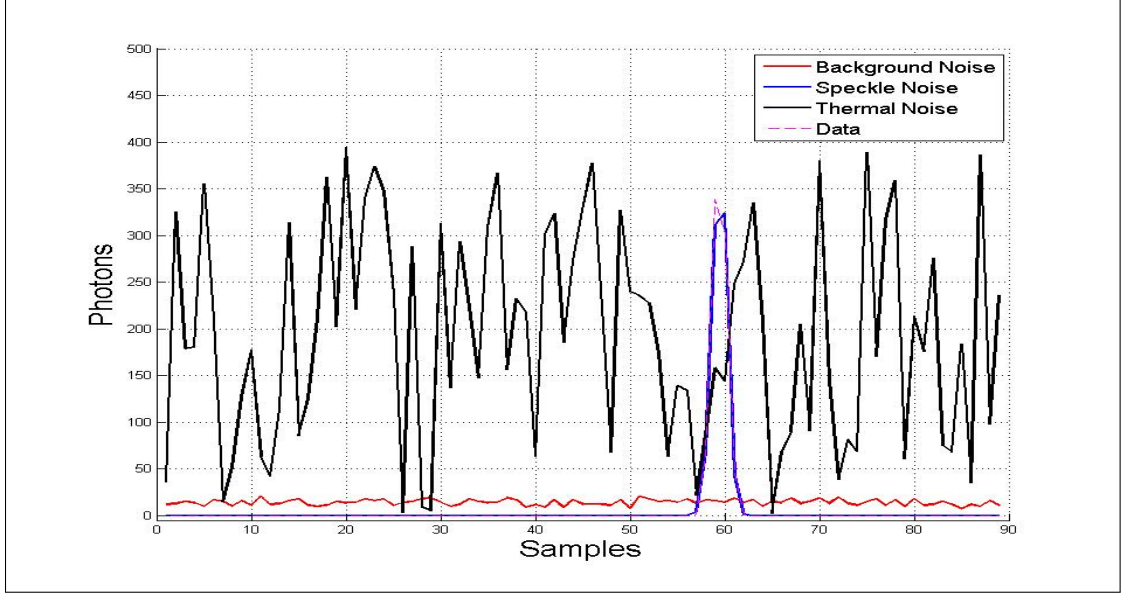


Figure 3.5: Noise functions.

with h representing Plank's constant, η is the efficiency of the detector, and Δt is the sampling period in the time domain. Once all the noise sources are added into the signal, it is converted back to watts for estimation.

Background noise is generated with Poisson distribution and an expected value of [11]

$$E[N_b] = \frac{S_{IB}\Delta_\lambda A_B \rho_t \eta \tau_a \tau_o D_R^2 \Delta t}{4R^2 h \nu} + E[N_{dark}]. \quad (3.16)$$

Background noise adds the least amount of noise to the system, but does limit the effectiveness of the APD in its effort to increase the SNR.

The photon counting and speckle noise is generated using a negative binomial distribution with variance [11]

$$\sigma_{speckle}^2 = E[N_p] \left(1 + \frac{E[N_p]}{M} \right), \quad (3.17)$$

where M is the degrees of freedom of the light and $\sigma_{speckle}^2$ is the variance of the measured photon counts driven by the noise. An M value of 90, used in the simulation, indicates the laser light is incoherent.

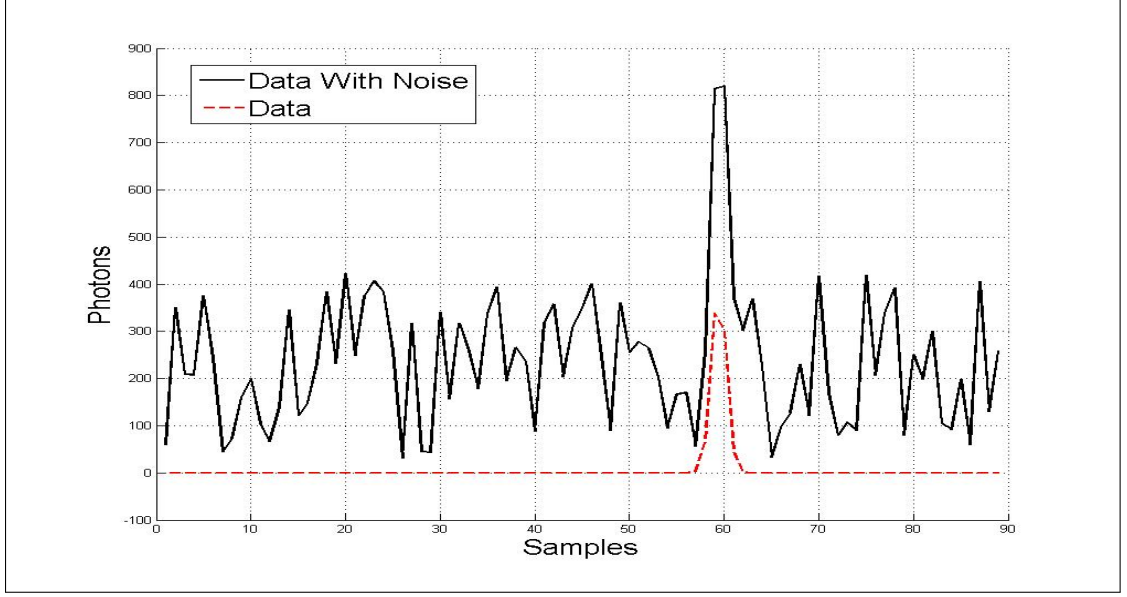


Figure 3.6: Noise comparison.

Thermal noise that is introduced into the LADAR system by the electrical components of the APD detector is described by Gaussian distribution with variance calculated as [11]

$$Q_n^2 = \frac{k_b T C}{q_e^2}. \quad (3.18)$$

Thermal noise is the most significant noise source for the signal. Fortunately, thermal noise is mitigated by using a gain characteristic of the APD detector.

The total signal is calculated by combining the noise and the true signal as

$$N_{total} = N_{background} + N_{thermal} + N_{speckle}, \quad (3.19)$$

where the variable $N_{speckle}$ is the speckle noise layered on top of the signal that was incident on the LADAR detector. The SNR of the data is controlled to a limited extent by [11]

$$SNR_{APD} = \frac{G_{apd} N_{max}}{\sqrt{Q_n^2 + G_{apd}^2 \sigma_{speckle}^2 + G_{apd}^2 N_b}}. \quad (3.20)$$

Because of the spatial Gaussian distribution of the energy contained in the reflected signal, a significant portion of the light reflected back towards the detector has a

very small amplitude. Therefore, an accurate SNR cannot be calculated because taking the average return across the entire range gate would produce a value not representative of the true signal. A representative value of the data is calculated by taking the maximum value of the signal for each pixel and averaging these values over the detector array to get N_{max} . To isolate the speckle noise from the variable $N_{speckle}$, the true signal is stripped off, represented by $N_s = N_{speckle} - N$. Then the square of the standard deviation of N_s gives the variance of the speckle noise, which is inserted into Equation (3.20).

3.2.4 Exclusion of Atmospheric and Optical Aberrations. The modeling of the atmospheric and optical aberrations were excluded from the LADAR model for two reasons. First, adding aberrations into the LADAR system complicates the estimation and simulation process. It is easier to understand the performance of the interpolators without adding additional factors into an already complicated process. Secondly, the exclusion of the optical aberrations is justified by describing the atmospheric coherence diameter (r_o). The variable describes the image degrading effects of the atmosphere on the image. The turbulence effects on the image are minimal when the relationship described $D_r > r_o$ is true [11], [20]. In this study's case, the values are listed in Table 3.1, justifying the exclusion of the optical aberrations in the LADAR model. The value for r_o of five centimeters is within the acceptable range and describes a relatively good seeing day through the atmosphere [20].

3.3 Estimation

Estimations on the simulated data of the LADAR were conducted using matched filters. The matched filter is implemented in a two step process to range the target and to determine the slope.

First, the range of the target was found using [27]

$$\rho = \frac{1}{N} \sum_{n=1}^N \frac{(d_n - \bar{d})(r_n - \bar{r})}{\sigma_d \sigma_r}, \quad (3.21)$$

comparing the data, d_n , with the generated reference waveforms, r_n . The mean value of the data and reference waveform is represented by \bar{d} and \bar{r} . The reference waveforms are generated using a two dimensional range equation driven by the Gaussian pulse model [11]

$$P_t(t) = \frac{E_t}{\sigma_w \sqrt{2\pi}} \exp\left[\frac{-(t)^2}{2\sigma_w^2}\right], \quad (3.22)$$

detailed in Section 2.1.1. The power transmitted to the target is inserted into the 2D range equation [11]

$$P_{det}(t) = \frac{\tau_o \tau_a^2 D_R^2 \rho_t (dA) P_t(t)}{R^2 \theta_R (\theta_t R)^2}. \quad (3.23)$$

The difference between the 3D range equation shown in Equation (3.11) and Equation (3.23) are the extra three terms of θ_t , R , and P_t . The two new terms of θ_t and R refers to the angular divergence of the laser beam. The angular divergence is compensated in the 3D equation by the Rayleigh-Sommerfeld propagation equation. The reference waveform P_t is identical to the 3D P_t (used in Equation 3.11) in pulse width, but is only roughly similar in amplitude. Due to the 3D spatial dispersion of the energy in the beam, the amplitude of the Gaussian pulse for each pixel in the detector array varies greatly. However, the shape of the pulse is the most important characteristic of the waveform because the estimation algorithm chosen relies on the correlation coefficient [27].

Once the range of the object is ascertained, the pulse width of the reflected pulse is estimated. The pulse width estimation leads to the calculation of the slope of the target. The reference waveforms for the pulse estimations are generated using [11]

$$P_{tot}(t_k) = \sum_{kk=1}^N P_{det}(t_k - t_{kk}) T_p(t_{kk}), \quad (3.24)$$

with T_p representing the target profile that was developed in the same manner as detailed in Section 3.2.2. To estimate the pulse width, a reference target profile is generated based on the angles listed in Table 3.3. With the estimated range kept the same, 14 different reference waveforms are generated and compared with the

data received using Equation (3.21). The slope of the target is calculated using the trigonometric relationship of a right triangle shown in Figure 3.4(b) with a known base (derived from the pixel size) and angle estimation.

Table 3.3: The search space angles of the target's slope.

	Degrees
Reference Angles	0, 30, 45, 60, 70, 72, 74, 76, 78, 80, 82, 84, 86, 88

3.3.1 Angle Estimation Reasoning. The calculation of the pulse width expansion is dependent on the sampling rate in the time domain, the pixel FOV at the target, and the slope of the target. The amount of target profile impulse returns depend on the sampling in time and the length of the surface slope in the longitudinal domain. When the surface slope contains small angles relative to normal, the change in the length of the longitudinal distance is small. Therefore, there is very little pulse width expansion when the surface angles are between 0 and 60 degrees. That leads to a sparse selection of angles to estimate for between 0 and 70 degrees. The reference angle selection rate increases from 70 to 90 degrees because of the increase in change with respect to the distance of the surface slope in the longitudinal domain.

In the event that different angles other than zero have an identical target profile due to a long sampling period in the time domain, the algorithm judging the correlation coefficient between the reference waveform and data waveform gives preference to the previous selection in the event of a tie. Therefore, if there is no pulse width expansion, the estimator will select a surface with zero degrees, even though it is possible to have a surface with a significant angle and reflect a Gaussian pulse with no detectable pulse width expansion.

3.4 Interpolation

The interpolation phase of the simulation involves taking the spatially down-sampled data from the estimation conducted in the simulation and interpolating the data to the original resolution of the image. This study uses two downsampling factors

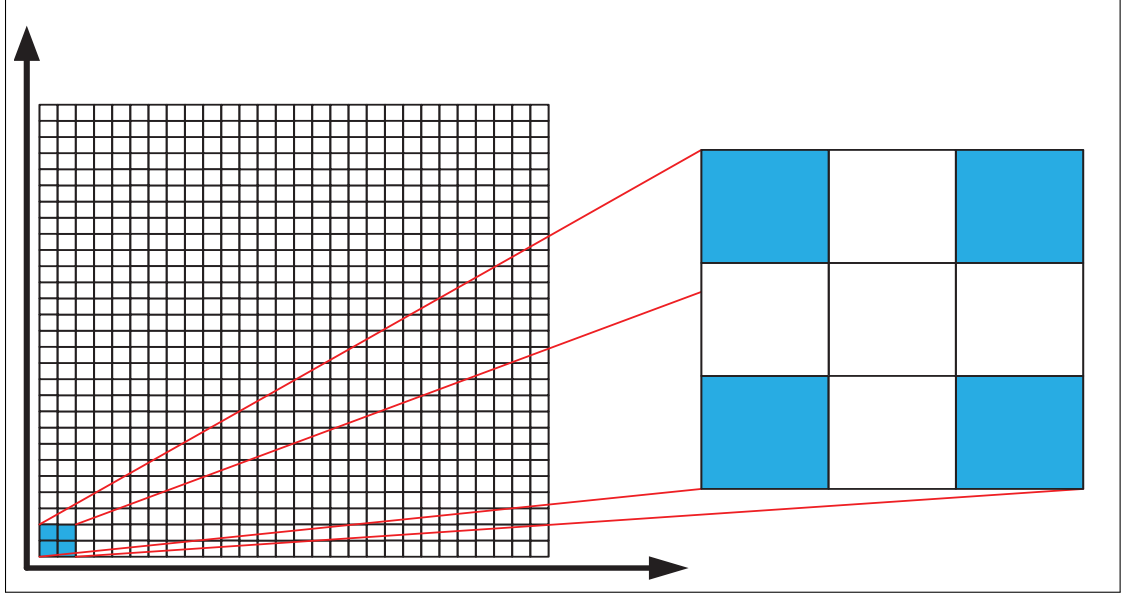


Figure 3.7: The 28 by 28 grid of sampled points is interpolated by a factor of two for comparison to the original image with a resolution of 56 by 56. The right side of the image shows four estimated data points in color and the interpolated points are in white.

which are listed in Table 3.1. As mentioned in Section 2.2, four different interpolators are used for comparison: a linear, cubic spline, sinc, and Hermite. The interpolators are used to increase the resolution of the sampled data back to the original size.

The bilinear and cubic spline interpolations in 3D are carried out with built-in software functions. The interpolation factor is determined by the amount of spatial down sampling of the signal conducted on the front end of the simulation. The 3D sinc interpolator is implemented using convolution. The 3D sinc filter is developed using

$$\text{sinc2}(x, y) = \text{sinc}(x)\text{sinc}(y), \quad (3.25)$$

where the sampling period is approximately $\pm 2\pi$ and the sampling interval is the inverse of the down sampling factor ($1/q$).

The bi-Hermite interpolator is implemented using

$$\begin{aligned}
p_{i,j}(u(x), v(y)) = & \sum_{\Delta i=0}^1 \sum_{\Delta j=0}^1 (f_{i+\Delta i, j+\Delta j}) \alpha_{\Delta i}(u) \alpha_{\Delta j}(v) \\
& + \sum_{\Delta i=0}^1 \sum_{\Delta j=0}^1 \Delta x_i \left(\frac{\partial f}{\partial x} \right)_{i+\Delta i, j+\Delta j} \beta_{\Delta i}(u) \alpha_{\Delta j}(v) \\
& + \sum_{\Delta i=0}^1 \sum_{\Delta j=0}^1 \Delta y_j \left(\frac{\partial f}{\partial y} \right)_{i+\Delta i, j+\Delta j} \alpha_{\Delta i}(u) \beta_{\Delta j}(v), \tag{3.26}
\end{aligned}$$

with the range estimations incorporated in all three double summations, the horizontal slope estimations incorporated in the second double summation, and the vertical slope estimations incorporated in the last double summation.

The implementation of the bi-Hermite interpolator is best explained in 2D with f and g_{grad} functions of x only. The estimation of the magnitude of a slope is possible, but not its direction or sign. The direction or sign is inferred by fitting a quadratic $q_i(x)$ to each sample f_i and its two immediate neighbors, $f_{i\pm 1}$. The sign of the true derivative is estimated as the sign of the derivative of the quadratic, therefore the derivative is estimated as

$$\hat{G}_{grad}(x_i) = \frac{q'_i(x_i)}{|q'_i(x_i)|} g_{grad}(x_i), \tag{3.27}$$

where $|\cdot|$ denotes the absolute value and we make the exception of $0/0 = 0$.

Similar to the 2D case, the 3D problem with adding direction to the slope is now introduced. The gradient of each sample in a 3D case is constructed by combining the known gradient magnitude with the orientation of the gradient of a pair of 2D quadratics $q_{i,j}(x)$, $p_{i,j}(y)$ fitted to the sample in question and its four immediate

neighbors, $f_{i\pm 1,j}$, $f_{i,j\pm 1}$,

$$\hat{G}_{grad}(x_i, y_j) = \frac{\left[\frac{\partial q_{i,j}}{\partial x}, \frac{\partial p_{i,j}}{\partial y} \right]^T}{\left\| \left[\frac{\partial q_{i,j}}{\partial x}, \frac{\partial p_{i,j}}{\partial y} \right]^T \right\|_{(x_i, y_j)}} g_{grad}(x_i, y_j), \quad (3.28)$$

where $\|\cdot\|$ denotes the Euclidean norm of a vector. For a uniformly spaced grid, Equation (3.28) reduces to

$$\hat{G}_{grad}(x_i, y_j) = \frac{[(f_{i+1,j} - f_{i-1,j}), (f_{i,j+1} - f_{i,j-1})]^T}{\sqrt{(f_{i+1,j} - f_{i-1,j})^2 + (f_{i,j+1} - f_{i,j-1})^2}} g_{grad}(x_i, y_j), \quad (3.29)$$

with $g_{grad}(x_i, y_j)$ representing the estimation of the magnitude of the gradient in Equations (3.27), (3.28), and (3.29).

3.5 Testing Effort

The purpose of the simulation is to test each interpolator's ability to accurately increase the resolution of sampled LADAR returns. The 3D LADAR simulation was run varying the following variables: range to target, sampling in time, sampling in space, and using nine different targets. In addition, each test was run 10 times due to the randomness of the noise functions. Also, the SNR of the signal was limited to three or greater, ensuring a strong estimation of range. The SNR is controlled using the APD mentioned in Section 2.1.8.

3.5.1 Target Creation and Down Sampling Implementation. Nine different targets were created using a combination of the four different target profiles discussed in Section 3.1.1. Each target profile shown in Figure 3.1 makes up four of the targets. Each of the next four targets contain a target profile shown in Figure 3.1 placed in nine different offset locations in the target plane. The ninth target consists of a few of each target profile placed throughout the target plane. The placement of the multiple target profiles had to be offset due to the down sampling process described below.

Two different spatial down sampling strategies were considered for the simulation. The first technique involved averaging the pixels together. The second technique down sampled the data by incrementing through the detector array and selecting every second or fourth pixel, depending on the down sampling rate. The former method is considered more realistic because the down sampling process includes all of the received reflected light. But the execution of this down sampling method lead to the skewing of objects to the left side of the image. Therefore, the latter down sampling technique was chosen.

The selection of the down sampling technique lead to the decision to offset the placement of the target profiles. If the target profiles were not offset, then certain interpolators could get an unintended advantage. For instance, consider the cone target profile, consistently placed throughout the target plane. The down sampling could possibly occur at the peaks of every cone, giving the linear and Hermite interpolators an unfair advantage. Therefore, the objects were placed slightly offset to counter this potential bias.

3.5.2 Root Mean Square Error. The images generated by the four interpolators are compared to the original control images described above in various ways. First, the RMSE is calculated by [24]

$$RMSE(\hat{\theta}) = \sqrt{\frac{1}{MN} \sum_{m=1}^M \sum_{n=1}^N |u(m, n) - u'(m, n)|^2}, \quad (3.30)$$

where u' represents the control image and u represents the interpolated image. The RMSE calculations of the images provide a measurement of how much each value of a pixel, on average, is off from the value of each pixel for the control image. In this study's case, the value of each pixel is the height of the surface for the object.

3.5.3 T-test. Besides the RMSE calculations, a T-test is utilized to analyze the performance of the interpolators. T-tests are used to look for differences in the

mean of two groups [28]. In this study's case, the T-test was implemented to determine whether a control image is significantly different from the interpolated image. There are two assumptions that have to be made about the data to apply the T-test. The data has to be independent and have a normal distribution. To utilize the T-test, certain parameters need to be established first. The criterion used for rejecting a null hypothesis, α , is defined as the probability of a Type I error or false positive. The variable α is often called the significance level or sensitivity and is represented by [28]

$$\alpha = P(\text{Type I error}) = P(\text{Reject } H_0 | H_0 \text{ is true}). \quad (3.31)$$

The choice of value for the significance level is arbitrary and is usually selected as 0.05 [28]. For this study, the α value is selected as 0.10. The t-test value is found by [28]

$$T = \frac{\bar{x}_T - \bar{x}_C}{\sqrt{\frac{\sigma_T^2}{n_T} + \frac{\sigma_C^2}{n_C}}}, \quad (3.32)$$

with n representing the total number of pixels, σ^2 is the variance, and \bar{x} is the mean of the pixels for that image. Once the value is found, it is used in the calculation of the p value, which is the probability of obtaining a test statistic (T) at least as extreme as the one that was actually observed, assuming the null hypothesis is true (H_0). The rejection of the null hypothesis occurs when the p-value is less than the significance level. The p-value is calculated by [28]

$$p_{value} = P(|T| \geq T_0), \quad (3.33)$$

were the value of T is the T-test calculation from Equation (3.32) and T_0 represents the same calculation generated from a table corresponding to the chosen value of α . Next, the specific application of the T-test to this study is explained.

The T-test will allow for certain conclusions to be made about the comparison of two images. But, before that is discussed, qualifying statements about the data must be made to validate the utilization of the T-test. First, the data that consists of

the two compared images are independent because each pixel is calculated separately. Secondly, the distribution of the data is normal due to the number of pixels considered. Each image consists of an array of pixels with size equal to 56 by 56 pixels, summing to a total of 3,136 pixels. The considerable number of pixels provided justification for using the central limit theorem to prove normal distribution.

A T-test is conducted based on the following

$$H_0 : \mu(\text{control}) - \mu(\text{interpolated}) = 0, \quad (3.34)$$

with an alpha value equal to 0.1. If the T-test value produces a rejection of the null hypothesis, then it is concluded that the image generated by the interpolator contains a mean pixel value that is different from the mean pixel value for the control image. This result is statistically significant. Therefore, it is interpreted that an interpolator that produces more rejections of the null performed worse than an interpolator that produced less rejections of the null hypothesis.

3.5.4 Survey. A survey is also used to compare the images generated by the interpolator with the control image using human interpretation. Utilizing a survey provides another way to interpret the performance of the interpolators. This study wants to mirror the way humans prefer certain images over others. The implementation of the survey is described next.

The construction of the survey began with planning the survey itself. The setup began with choosing a set of images that were generated by the interpolators during one of the multitude of simulations. Then the control image for that simulation was selected for comparison. The four interpolated images are randomly placed on a single page next to the following identifiable letters: A, B, C, and D. Then, the participant is asked to judge the quality of the images compared to the control image. Each interpolated image is judged on a scale of one through four, with one being the best image and four being the worst. The survey was conducted using 19 participants

and eight different sets of images. The same question was asked for all eight sets of images.

The purpose of the survey is to get a human perspective on the performance of the interpolators. To achieve this goal, eight total sets of interpolated images were chosen for the survey. The first four sets were selected based on the requirement that they have the same simulation conditions, with the one exception being the target. The last four sets were chosen based on their RMSE results. Among the last four sets, two sets were chosen with favorable and unfavorable results for the Hermite interpolator, and two sets were chosen based on relatively even RMSE calculations for all four interpolators. The intention behind the selection methodology was to establish a good sample from the thousands of interpolated images produced from the tests.

3.5.5 LADAR Model Adjustments. The testing process of changing the range to the target requires addressing the LADAR model. Due to the physical nature of light, decreasing the target range from 10,000 to 4,000 meters decreases the FOV of the pixels. In the initial testing phase, the size of the pixel at the detector was determined to be 50 μm . Based on the following relationships described below, the FOV area for a single pixel is calculated by [11]

$$\gamma = \frac{\Delta}{f_l}, \quad (3.35)$$

$$A_{FOV} = (\gamma \cdot Z)^2, \quad (3.36)$$

with Δ representing the pixel size of the detector, f_l is the focal length of the LADAR, and Z is the range to target. Given that the detector size is a fixed 56 by 56 array, the FOV downrange of the detector is 2.8 meters for a target range of 10 km. Therefore, the targets for the LADAR simulation are constructed with the knowledge that the area of the FOV for the detector is a certain size. But, since the range to target is a dynamic variable in the LADAR simulation, other LADAR conditions have to be negotiated.

Table 3.4: Variable parameters of LADAR simulation dictated by the range to target.

Range (m)	Pixel Size (μm)	Target Size (m)	Beam Size (m)
10,000	50	2.80	10.47
9,000	45	2.52	9.42
8,000	40	2.24	8.37
7,000	35	1.96	7.33
6,000	30	1.68	6.28
5,000	25	1.40	5.23
4,000	20	1.12	4.19

Due to sampling constraints throughout the simulation, the relationship that could be exploited with the least amount of changes made to the LADAR simulation conditions was the pixel size at the detector. Adjusting the pixel size depending on the range requires changing the target size down range. But, this enables the sampling to remain consistent. Also, the beam waist of the LADAR pulse did not have to be adjusted because the relationship that dictates the size of the FOV for each pixel is consistent with the relationship described in Equation (2.4). The pixel, target, and beam size values are calculated for each different range to target and are listed in Table 3.4. The beam size is the diameter of the Gaussian beam at the target.

3.6 Chapter Summary

This chapter covered the implementation of the LADAR model, the simulation procedures, and the types of tests that were run on the data. The LADAR model was constructed piecemeal starting with the laser pulse, incorporating light propagation with target interaction, adding noise, and including the APD detector characteristics. The model was finished by explaining the estimation processes of the system. A brief explanation was provided on how the three basic interpolators were implemented. Also, a more in depth description of the bi-Hermite interpolator was provided to explain the unique application of the interpolator. Finally, the testing account was given to show the different ways of evaluating the performance of the interpolators. Next, Chapter IV displays the results of the performance of the interpolators.

IV. Results and Analysis

This chapter details results from the simulations described in Chapter III. First, the survey results are displayed in a frequency table and compared against a corresponding RMSE table. Then, the T-test results are shown in Section 4.2. The RMSE results derived from the multiple simulations ran across multiple conditions mentioned in Section 3.5 are discussed in Section 4.3. An analysis of the Hermite algorithm is conducted in Sections 4.4 and 4.6. The estimation efforts and their performance are covered in Section 4.5.

Before going further, a reference table is shown to reference the image number with the actual target shape.

Table 4.1: Target reference table.

Target Number	Target Description
Target 1	Single Dome
Target 2	Multiple Domes
Target 3	Single Cone
Target 4	Multiple Cones
Target 5	Single Square
Target 6	Multiple Squares
Target 7	Single Trapezoid
Target 8	Multiple Trapezoids
Target 9	Multiple Shapes

4.1 Survey Results

The survey results are reported in Table 4.2. All 19 participant surveys were decoded, summed, and then divided to get the percentages shown. Each row and column sums to one with possible error introduced from rounding to the nearest integer.

The images created by the Hermite interpolator are clearly preferred by most of the participants. The Hermite interpolated images were classified as among the best two images in the set of four 83% of the time. This result is consistent with the RMSE calculations of the same eight sets of images shown in Table 4.3. The Hermite

Table 4.2: Human subject survey results.

Interpolator	Best (1)	Second Best (2)	Second Worst (3)	Worst (4)
Hermite	41%	42%	11%	6%
Linear	34%	29%	26%	11%
Sinc	20%	21%	45%	13%
Spline	7%	7%	16%	71%

Table 4.3: RMSE results. Percentages are rounded to nearest integer.

Interpolator	Best (1)	Second Best (2)	Second Worst (3)	Worst (4)
Hermite	38%	50%	13%	0%
Linear	25%	25%	50%	0%
Sinc	38%	0%	38%	25%
Spline	0%	25%	0%	75%

interpolated images produced the lowest two RMSE results when compared against their peers 88% of the time. The percentages reported also suggest that the Hermite interpolator is resilient despite the varied shapes, with only 6% of the Hermite images classified as the worst in the set of four by the survey participants.

The linear interpolator results reported by Tables 4.2 and 4.3 are similar to the Hermite results. The sinc interpolator performed the best in comparison with the other interpolators a significant percentage of the time, reported by the frequency tables with 20% and 38%. The spline interpolator performed the worst among the four interpolators when considering the results from the two frequency tables.

As reported by Section 3.5.4, eight sets of images were selected for the survey. Out of the eight sets, four were selected with identical conditions set during the simulation. The control images used for comparison against the sets of interpolated images are shown in Figure 4.1. The RMSE values for the sets of four interpolated images are plotted against the varied sample rate and are shown in Figure 4.3 through Figure 4.6. The RMSE values reported in the figures are calculated by averaging all RMSE values for every test that occurs at that particular sample rate. The dashed lines seen in the figures represent the RMSE of an interpolated image with perfect estimations of the range and pulse width. The dashed lines represent the ceiling for

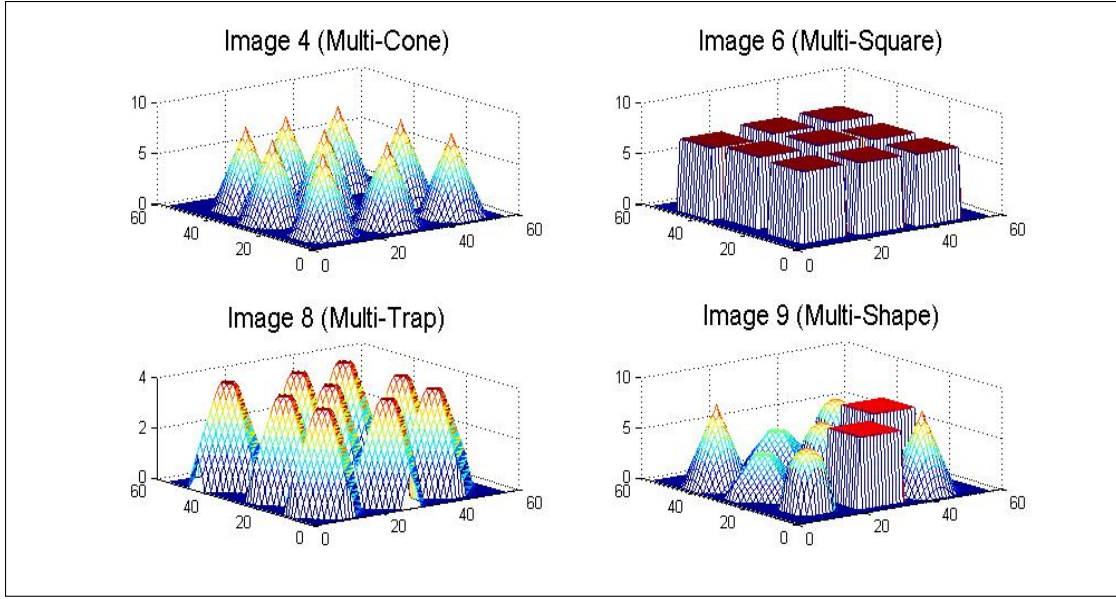


Figure 4.1: Control images related to survey and RMSE plots in Figures 4.3 through 4.6. Notice the offset placement of the shapes, mentioned in Section 3.5.1.

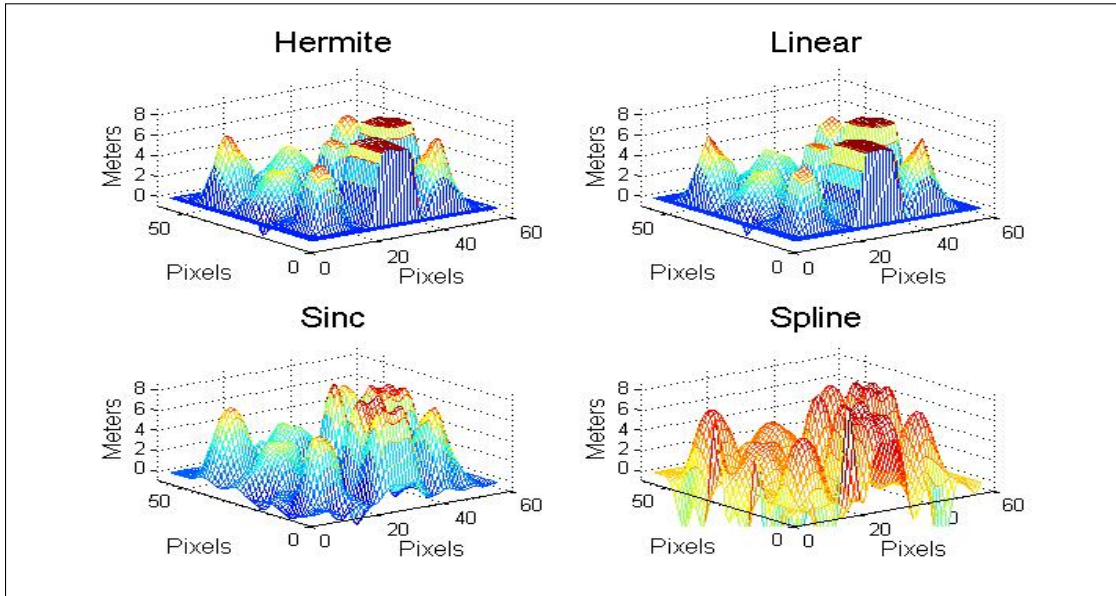


Figure 4.2: One set of interpolated images included in the survey. The figure shows each interpolator's attempt to reconstruct Target 9, shown in Figure 4.1, using SLR data estimates. The survey images were taken from the first sample rate in time and the RMSE values are shown in Figure 4.6.

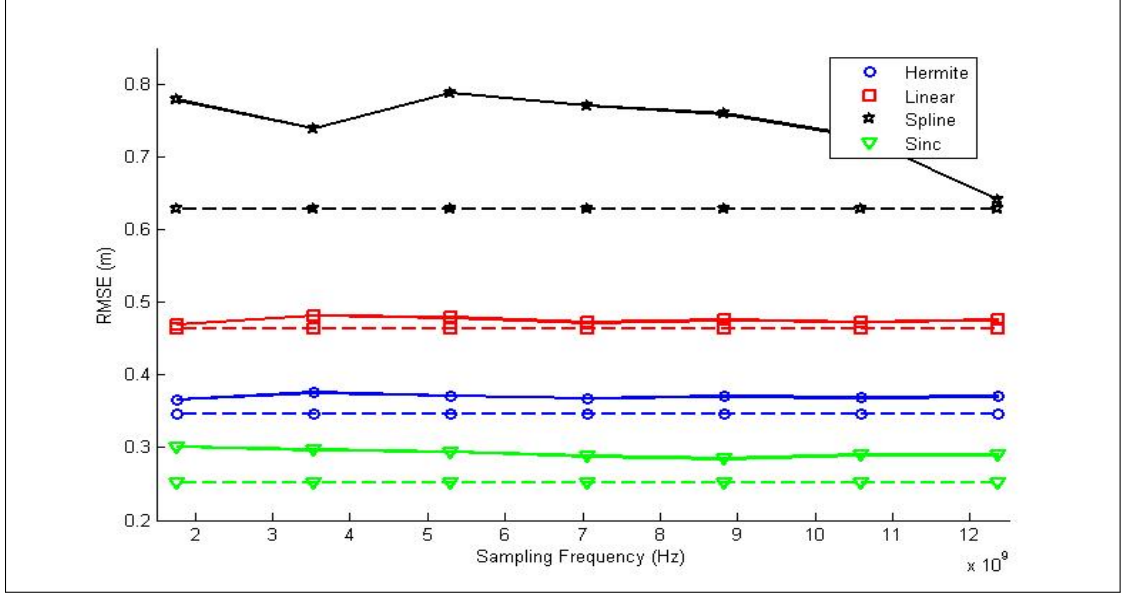


Figure 4.3: Target 4 (Multi-Cone) results. The dashed lines represent the RMSE of an ideal estimation and the solid lines represent the actual estimations.

the RMSE based performance of the interpolators. A summary of the RMSE plots shown in Figure 4.3 through Figure 4.6 is explained below.

The Hermite interpolator RMSE values are consistently among the lowest in comparison against the other interpolators. The sinc interpolator does well with cone and trapezoidal objects, rating as the best interpolator for these images. The spline interpolator is clearly the worst of the four interpolators based on the RMSE plots. The linear interpolator performance is right around the middle in comparison against the other interpolators. An example of one set of interpolated images used in the survey is shown in Figure 4.2. The averaged RMSE results for this set of images shown is reported by the first time sampling rate of the plot shown in Figure 4.6.

4.1.1 Resiliency of Interpolators. The average RMSE difference between the interpolated images using actual estimations of range and pulse width and interpolated images using perfect estimations of range and pulse width are shown in Table 4.4. The linear, spline, and sinc interpolators all use the same range estimations. The Hermite interpolator uses the same range information and also includes the

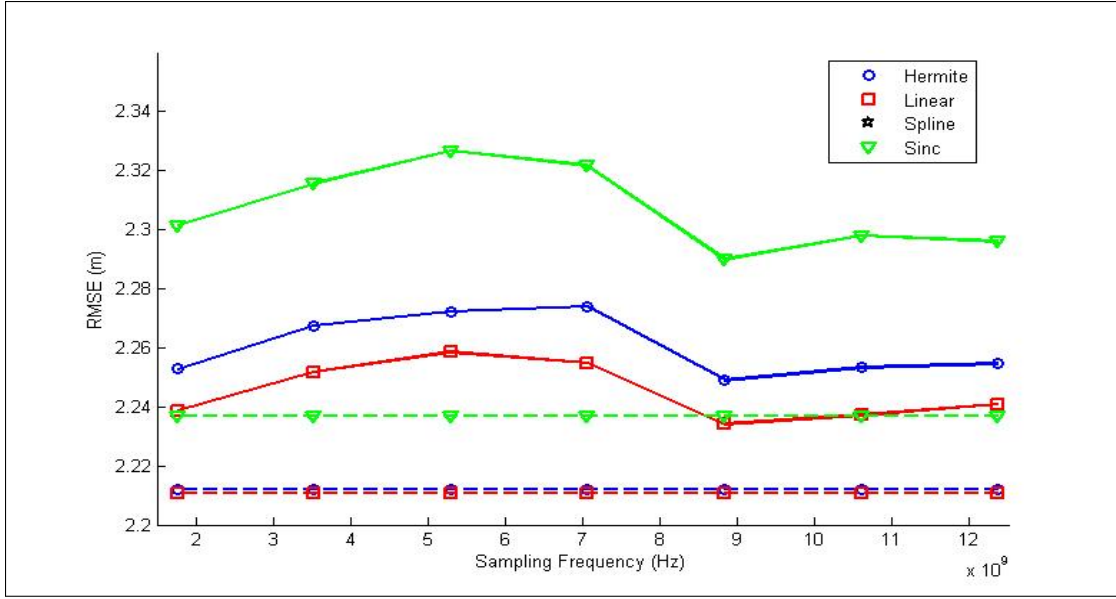


Figure 4.4: Target 6 (Multi-Square) results. The dashed lines represent the RMSE of an ideal estimation and the solid lines represent the actual estimations. The spline plot was centered around an RMSE value of 4, and isn't shown so more attention is applied to the higher performing interpolators.

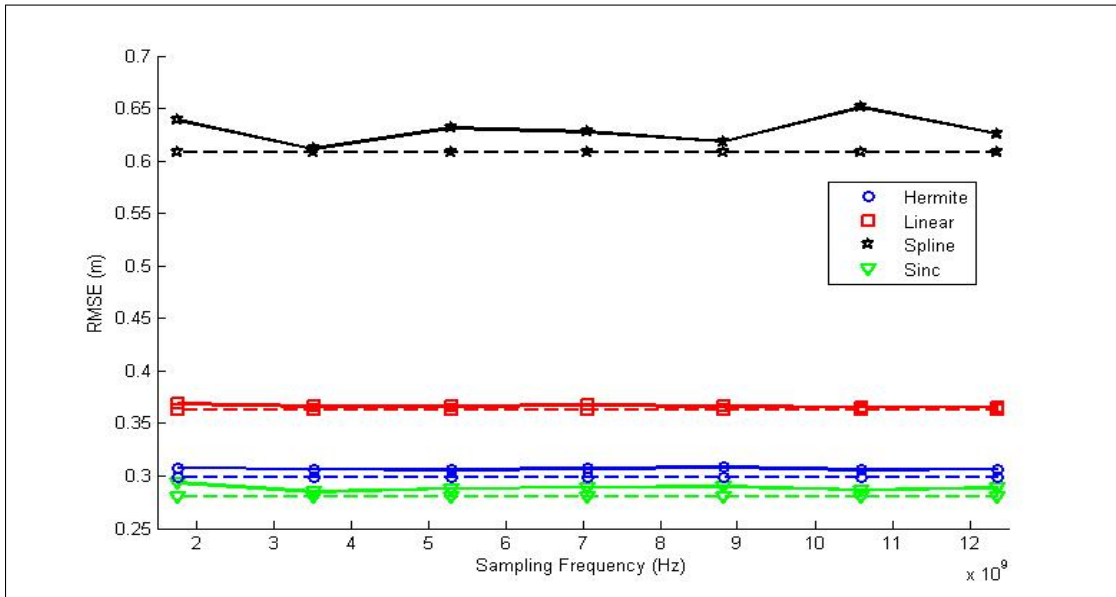


Figure 4.5: Target 8 (Multi-Trap) results. The dashed lines represent the RMSE of an ideal estimation and the solid lines represent the actual estimations.

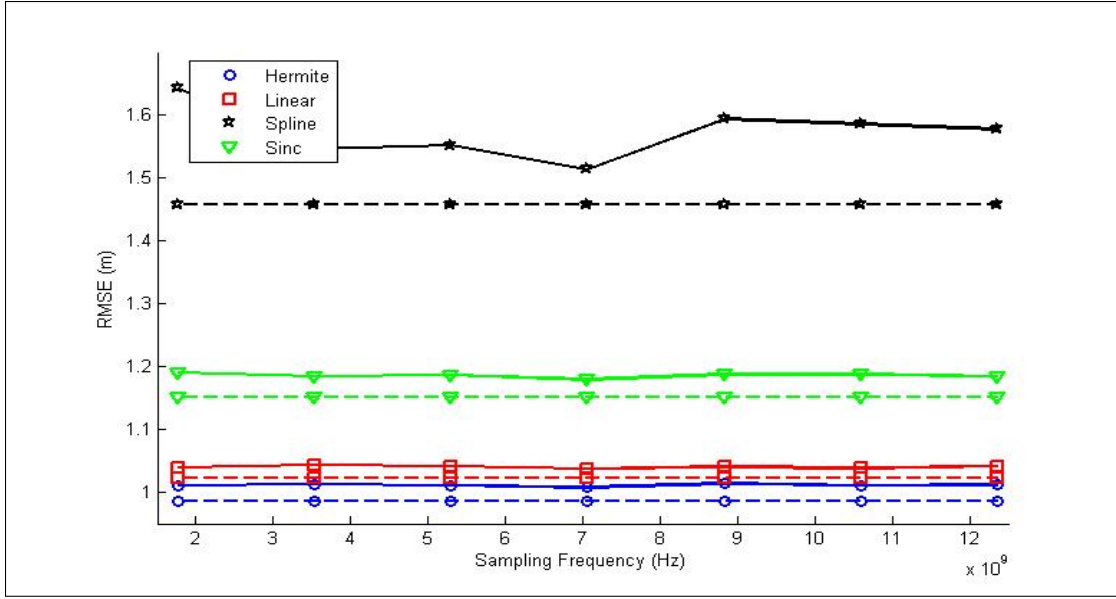


Figure 4.6: Target 9 (Multi-Shape) results. The dashed lines represent the RMSE of an ideal estimation and the solid lines represent the actual estimations.

Table 4.4: Mean of the difference in RMSE between ideal and actual estimation performance. Values in table are calculated by taking the difference between the dashed and solid line for each interpolator in Figures 4.3 through 4.6 and taking the average.

Interpolator	Image 4	Image 6	Image 8	Image 9
Hermite	0.023	0.048	0.008	0.026
Linear	0.012	0.034	0.004	0.017
Sinc	0.114	0.118	0.020	0.116
Spline	0.041	0.071	0.008	0.034

pulse width expansion estimations as well. The linear interpolator performs closest to its ideal performance when compared against the other three interpolators. The Hermite interpolator performs well in comparison with the other three interpolators, but includes additional data from the pulse width expansion estimation, introducing more potential for error. This possibly explains some of the difference between the performance of the linear interpolator and the Hermite interpolator. Despite this additional source of possible errors from the pulse width expansions estimation, the Hermite interpolator appears resilient against poor estimates in comparison to the other interpolators.

Table 4.5: Hypothesis test at range to target of 10 kilometers. The columns represent different FWHM values of the Gaussian pulse in time. The confidence interval was set at 0.10 for T-tests. The percentages reflect how often the null hypothesis was rejected.

Image Test	1 ns	2 ns	3 ns	4 ns
$H_1 : \mu(\text{control}) - \mu(\text{Hermite LR}) \neq 0$	14.3%	17.5%	30.2%	27.0%
$H_1 : \mu(\text{control}) - \mu(\text{Hermite SLR}) \neq 0$	12.7%	15.9%	20.6%	24.8%
$H_1 : \mu(\text{control}) - \mu(\text{linear LR}) \neq 0$	14.3%	17.5%	30.2%	27.0%
$H_1 : \mu(\text{control}) - \mu(\text{linear SLR}) \neq 0$	15.9%	22.2%	22.2%	25.4%
$H_1 : \mu(\text{control}) - \mu(\text{spline LR}) \neq 0$	12.7%	15.9%	31.8%	27.0%
$H_1 : \mu(\text{control}) - \mu(\text{spline SLR}) \neq 0$	34.9%	33.3%	41.3%	36.5%
$H_1 : \mu(\text{control}) - \mu(\text{sinc LR}) \neq 0$	15.9%	14.3%	23.8%	27.0%
$H_1 : \mu(\text{control}) - \mu(\text{sinc SLR}) \neq 0$	28.6%	31.8%	30.2%	33.3%

4.2 Hypothesis Testing

The hypothesis test was conducted on targets ranged at 10 kilometers. The results are found in Table 4.5. The percentages listed in the table were calculated by summing the total number of false positives and dividing by the total number of tests. A rejection of the null hypothesis implies the interpolated image does not accurately represent the control image. The results reported suggest that the Hermite interpolator clearly outperforms the other interpolators when comparing the images produced using SLR estimates. In fact, the Hermite interpolator performs slightly better using data from the lowest resolution estimates. At the very least, it suggests that the interpolator is resilient and the performance of the interpolator doesn't drop off significantly as the spatial sampling rate approaches the Nyquist criterion.

The author recognizes the potential error in the comparison. It is possible that the mean difference between two compared images can be zero without being the same image. A more applicable example for this application of the hypothesis test is the ringing effects sometimes produced by the interpolators. It is possible that there is relatively equal amounts of ringing above and below the control image profile, averaging out to zero, and therefore not producing a false positive. But, the T-test results are consistent with the survey and RMSE calculations, therefore, the

author believes the integrity of the test is legitimate and provides further proof of the performance of the Hermite interpolator.

4.3 General RMSE Results

The tables and figures in this section display the RMSE results over different tests. First, the interpolators are compared against each target profile. Then, the interpolators are compared over the different sampling rates in the time domain. Lastly, the mean RMSE values are plotted for each interpolator using LR estimates. The *standard deviation* (SD) of the RMSE results are plotted as well to see the deviation spread from the mean.

4.3.1 Target RMSE Analysis. The plots of each interpolator's performance for each target are shown in Figures 4.7 and 4.8. Each point in the plot represents the average of the RMSE for each interpolator's attempt for each target, calculated from 1,960 different tests.

Its clear that the interpolators struggled with Target 6, the multiple squares. This makes sense due to the high spatial frequency nature of the target. It is also clear that the spatial sampling was appropriate when comparing the results between the two estimate rates. The increase between the average RMSE results was approximately two, which is consistent for the other targets as well. This result justifies the spatial sampling approximation concluded in Sections 3.1.1.

Due to the overall poor performance of the spline interpolator, its hard to see the performance difference between the other interpolators, therefore, the average RMSE data is shown in Table 4.6. The author views target nine as the most realistic target due to its many different shape profiles. When comparing the results of the realistic target in Table 4.6, the Hermite interpolator error calculation is the least among the group of interpolators. In addition, the Hermite interpolator is the number one performer 61.1% of the time, and among the top two performers 83.3% of the time when considering data from Table 4.6.

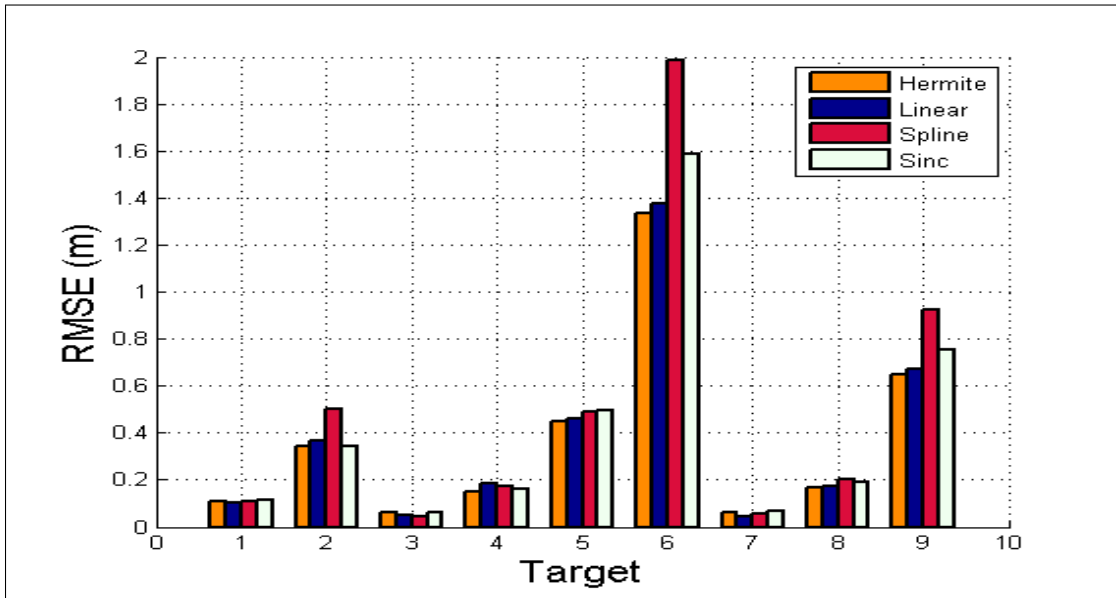


Figure 4.7: LR interpolator RMSE comparisons across all nine targets.

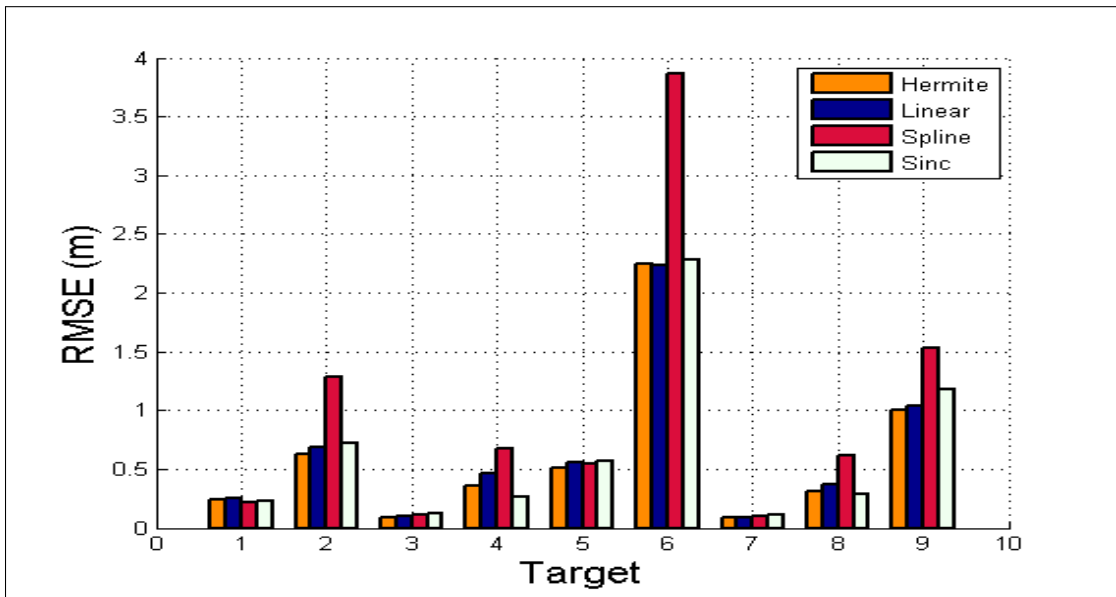


Figure 4.8: SLR interpolator RMSE comparisons across all nine targets.

Table 4.6: Shows the averaged RMSE values of each interpolator against each constructed target used in the simulations.

Targets	1	2	3	4	5	6	7	8	9
Hermite LR	0.106	0.342	0.060	0.148	0.449	1.336	0.064	0.165	0.645
Hermite SLR	0.237	0.632	0.091	0.362	0.506	2.250	0.083	0.306	1.006
Linear LR	0.104	0.368	0.049	0.185	0.462	1.376	0.047	0.175	0.671
Linear SLR	0.256	0.682	0.095	0.468	0.561	2.235	0.083	0.365	1.035
Sinc LR	0.116	0.344	0.060	0.163	0.493	1.584	0.065	0.192	0.754
Sinc SLR	0.227	0.721	0.124	0.269	0.570	2.286	0.116	0.282	1.174
Spline LR	0.109	0.501	0.046	0.171	0.489	1.983	0.054	0.204	0.922
Spline SLR	0.218	1.289	0.108	0.674	0.548	3.862	0.097	0.620	1.536

4.3.2 Time Sampling Rate RMSE Analysis. For time sample comparison plots, each interpolator's average and SD of the RMSE are graphed. Each data point calculation involves 2,520 different tests. Only the average RMSE results produced from the LR estimates are plotted because the RMSE results produced from the SLR estimates were very similar in comparison and did not show anything of note. Due to close comparisons between the interpolators, the average RMSE calculations for both sets of estimates are shown in Table 4.7.

The data plotted against the sampling rate in the time domain, shown in Figures 4.9 through 4.12, use the Nyquist sampling scale to define the horizontal axis. The Nyquist sampling scale is defined by

$$N_{scale} = \frac{f_{actual}}{f_{Nyquist}}, \quad (4.1)$$

where f_{actual} represents the different sampling rates used and $f_{Nyquist}$ is the Nyquist criterion sample rate in the time domain. The Nyquist criterion sample rate is the standard deviation of the Gaussian pulse transmitted from the LADAR, covered in Section 2.3.1. The Nyquist sampling scale allows us to combine the data simulated using different FWHM values, and therefore different sampling rates, on the same graph. Values less than one on the Nyquist scale indicates undersampled data. Values of more than one indicates oversampling.

Once again, the Hermite interpolator is at the top of any comparisons made between the other interpolators. However, the Hermite interpolator's performance tends to worsen as the sampling rate increases. This is especially of note since this is not the case with the other interpolators. The negative trend is due to the decrease in accuracy of the pulse width estimates as the sampling rate in the time domain increases. Further explanation of the negative Hermite performance trend is explained in Section 4.5.

Table 4.7: Shows the averaged RMSE values of each interpolator using SLR spatial sampling estimates against the different sampling rates in the time domain. The SD of the results is listed as well.

Nyquist Scale	0.75	1.25	2.25	3.00	3.75	4.50	5.25
Hermite Mean	0.608	0.608	0.605	0.606	0.609	0.609	0.611
Hermite SD	0.410	0.409	0.416	0.416	0.412	0.413	0.412
Linear Mean	0.647	0.647	0.640	0.641	0.641	0.641	0.640
Linear SD	0.395	0.393	0.400	0.400	0.399	0.399	0.400
Sinc Mean	0.646	0.641	0.642	0.640	0.639	0.638	0.640
Sinc SD	0.440	0.440	0.447	0.447	0.445	0.445	0.447
Spline Mean	1.009	0.999	0.993	0.989	0.993	0.988	0.992
Spline SD	1.242	1.243	1.248	1.262	1.271	1.249	1.268

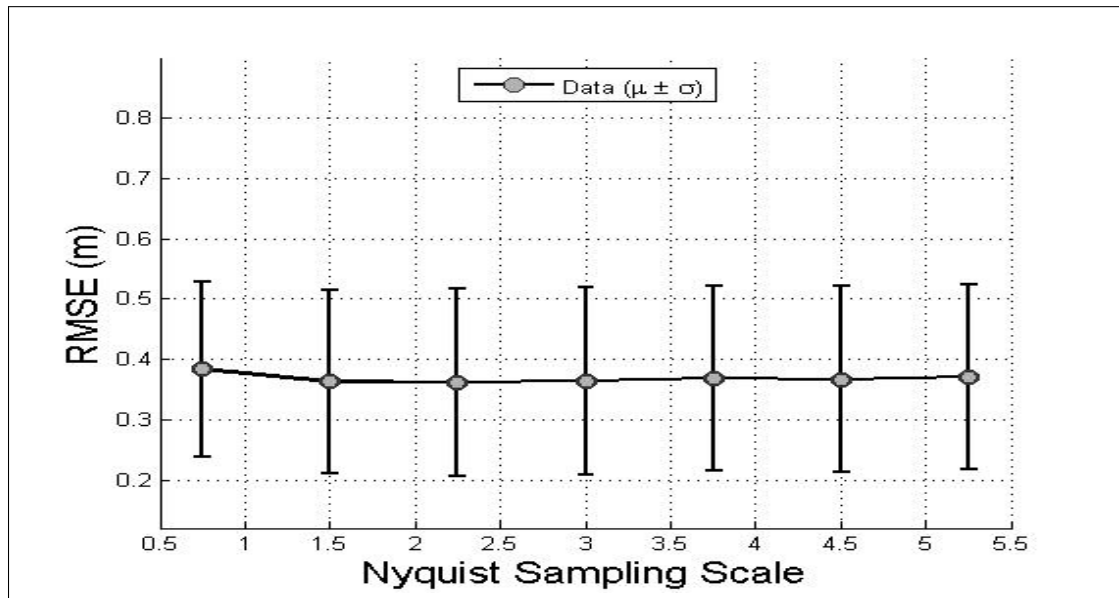


Figure 4.9: LR Hermite interpolator RMSE average plotted against the sampling rate in the time domain.

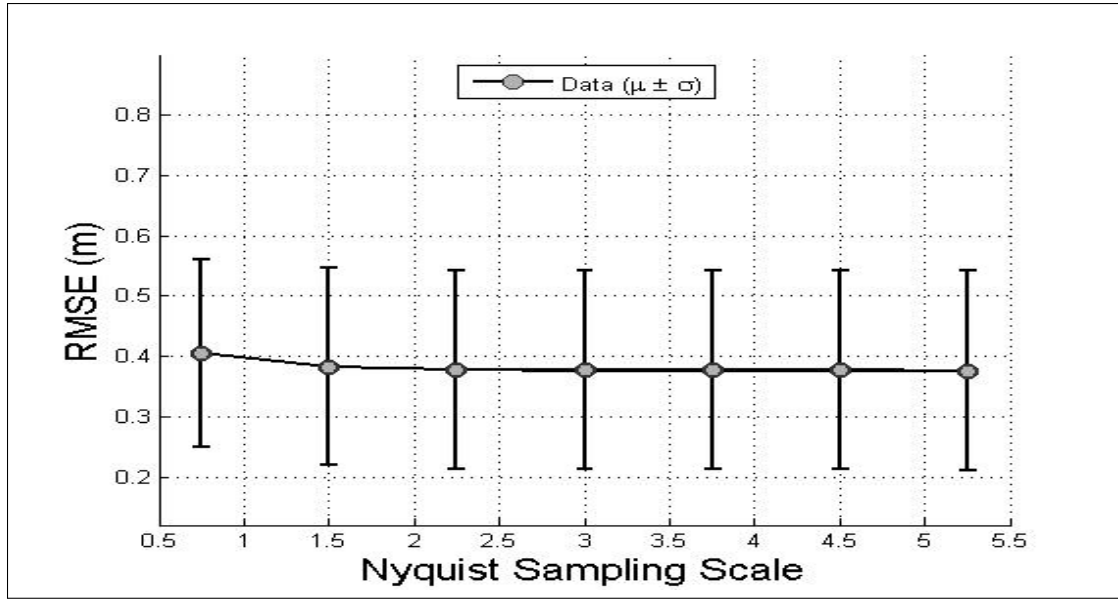


Figure 4.10: LR linear interpolator RMSE average plotted against the sampling rate in the time domain.

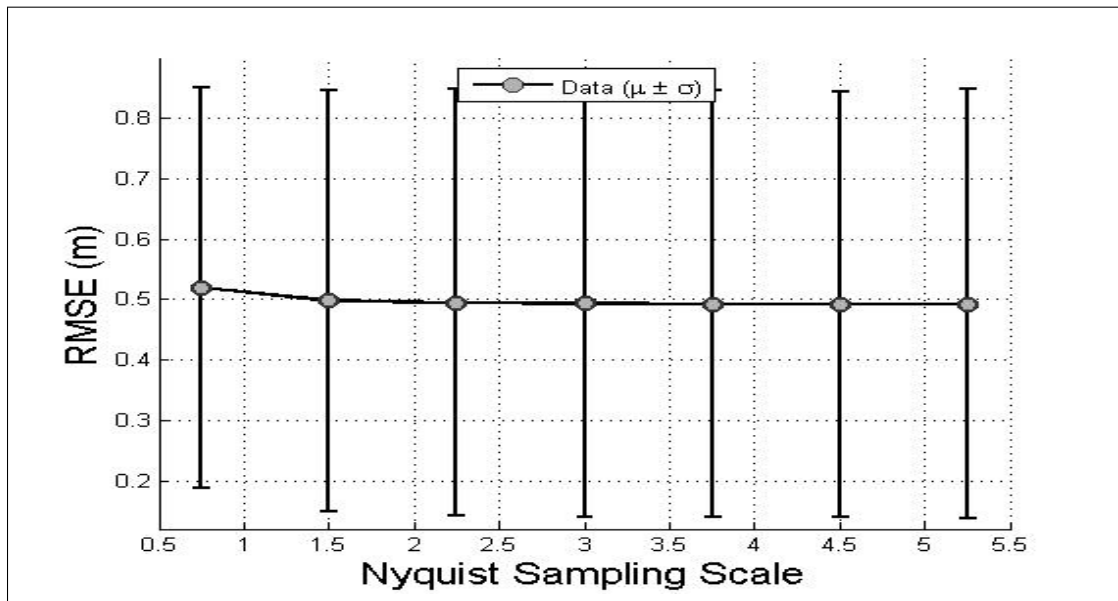


Figure 4.11: LR spline interpolator RMSE average plotted against the sampling rate in the time domain.

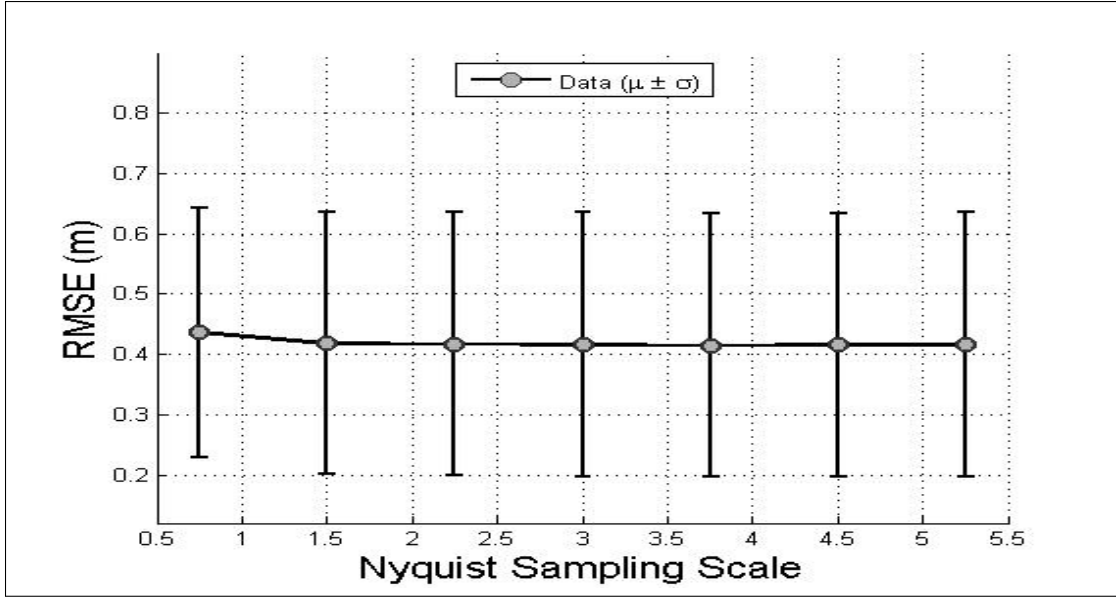


Figure 4.12: LR sinc interpolator's RMSE average plotted against the sampling rate.

4.4 Adjustment of Bi-Hermite Algorithm

The initial implementation of the bi-Hermite interpolator was a challenge. Because of the initial lack of positive results, many iterations of tests and evaluations were attempted to find the source of error. Over the process of these iterations, positive results were finally realized, showing proof of the concept for the Hermite interpolator. But, in the process, a change in the Hermite algorithm was unintentionally coded. Originally the magnitude of the slope of the target was folded into the Hermite algorithm using the tangent of the radian value derived from the slope estimation. The unintentional change in code eliminated the tangent of the radians, and instead included just the radian estimate into the algorithm. This change effectively reduced the influence of the gradient magnitude in the bi-Hermite equation.

Unfortunately, the evaluation process did not reveal the source of the positive results until after the simulations were conducted. But, the obvious question arose about whether the substitution of the slope angle for the magnitude of the gradient was ideal. To test this, the Hermite interpolator was evaluated using ideal estimates of the

data to measure the performance curve of the interpolator. The test was conducted using each target profile. The tests were run using the following equations for the variable representing the magnitude of the slope for the surface of the target;

$$g(x, y) = \tan(\theta), \quad (4.2)$$

$$g(x, y) = \theta, \quad (4.3)$$

$$g(x, y) = D_{scale} \tan(\theta), \quad (4.4)$$

where Equation (4.2) represents the first iteration of the Hermite algorithm, Equation (4.3) represents the equation that was used to generate all previous results shown in Chapter IV, and Equation (4.4) is the scaled version of the first iteration. The results of the tests are shown in Figure 4.13. The choice for scaling values was based on rough RMSE calculations and the trending performance of the curve. The scaling factors are implemented by multiplying the tangent of the estimated radians in the Hermite algorithm.

Based on the mean results shown in Figure 4.13, the performance of the Hermite interpolator peaked as the scaling factor was reduced to a value of 0.25. The interpolator performance began to deteriorate as the scaling factor continued to be reduced. Therefore, a small test set was run using the scaling factor for 0.25 to gauge the performance of the adjusted interpolator compared to the original Hermite algorithm using only radians for the magnitude of the gradient.

The simulation was run using a target distance of 10 km and a FWHM pulse width of 4 ns. The comparison of the two Hermite interpolators is shown in Figure 4.14. On average, the new Hermite algorithm using Equation (4.4) with a 0.25 scaling factor offered an additional 8% improvement in the RMSE average. The improvement was consistent between the LR and SLR estimates. A sample comparison of the interpolator efforts to construct target nine from the SLR estimates is shown in Figures 4.14 and 4.15. The target constructed using the scaling factor of 0.25 pro-

duced a more accurate image based on the RMSE results, with a mean improvement of 8.3% for target nine. The image shown in Figure 4.14 displays more overshoot for one of the square objects, but possibly maintains the integrity of the majority of object profiles better than the original Hermite interpolator (see cone and dome objects).

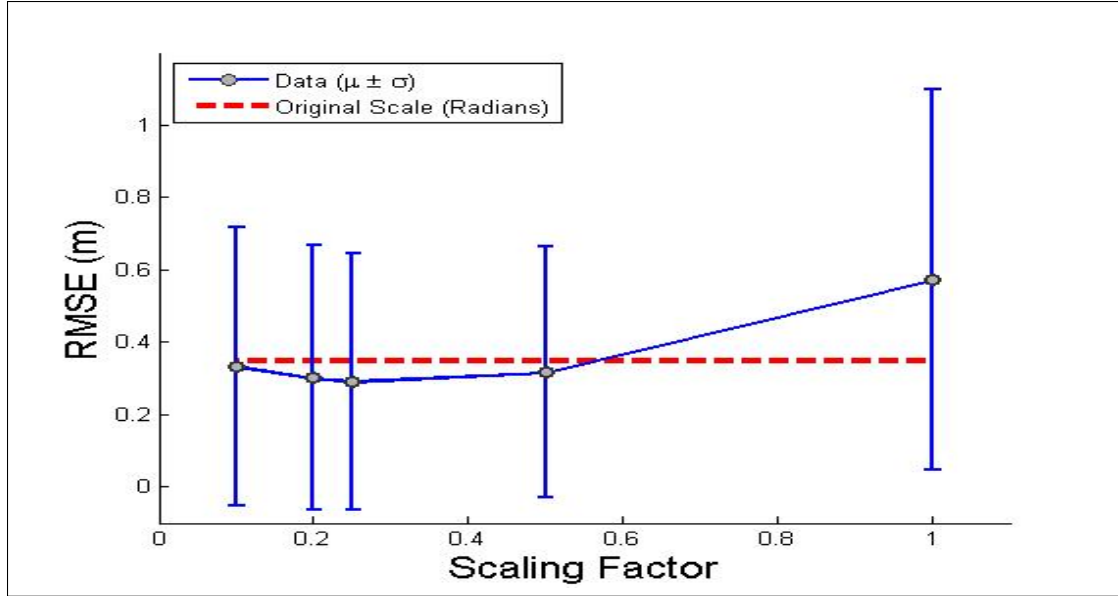


Figure 4.13: The RMSE of each scaling factor of the Hermite function concerning the magnitude of the gradient. The dotted line represents the Hermite performance using Equation (4.3). The right most data plot represents the Hermite performance using Equation (4.2). The data plots below the red line were calculated using Equation (4.4) in the Hermite algorithm.

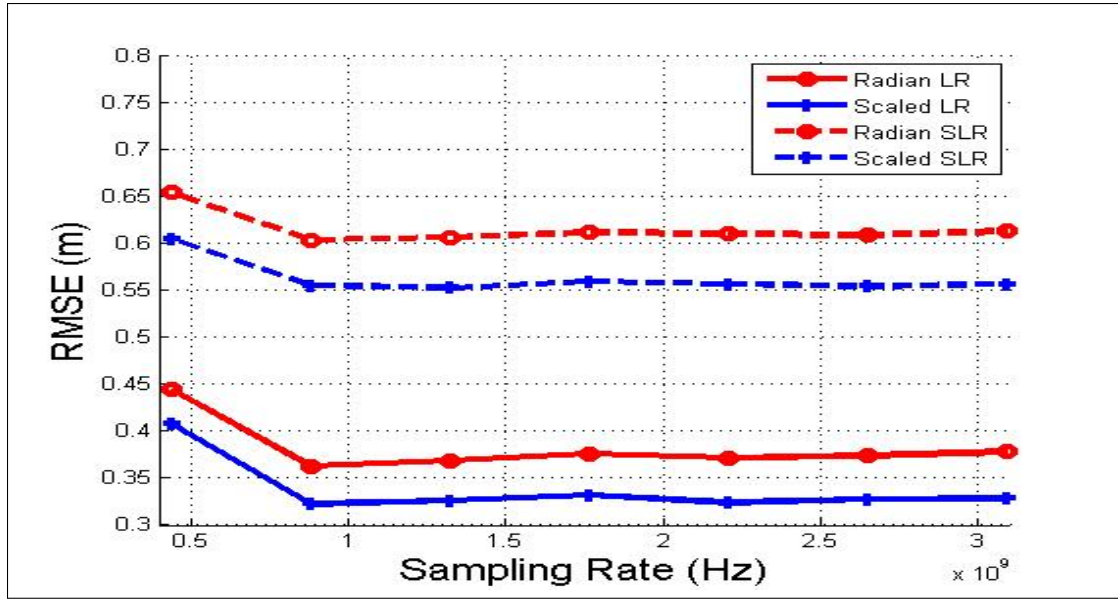


Figure 4.14: RMSE comparison between the Hermite algorithm that used slope angle (Equation (4.3)) and the Hermite algorithm that used the scaled magnitude of the slope of the target (Equation (4.4)). The scaling factor is 0.25.

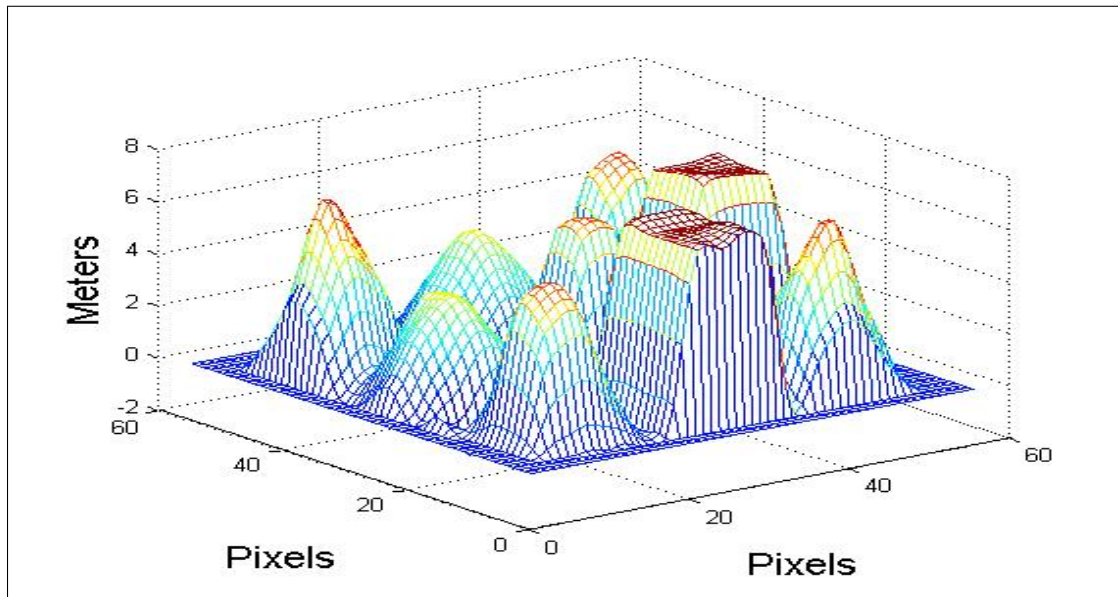


Figure 4.15: Interpolation of target nine using SLR estimates and the bi-Hermite algorithm using radians for magnitude.

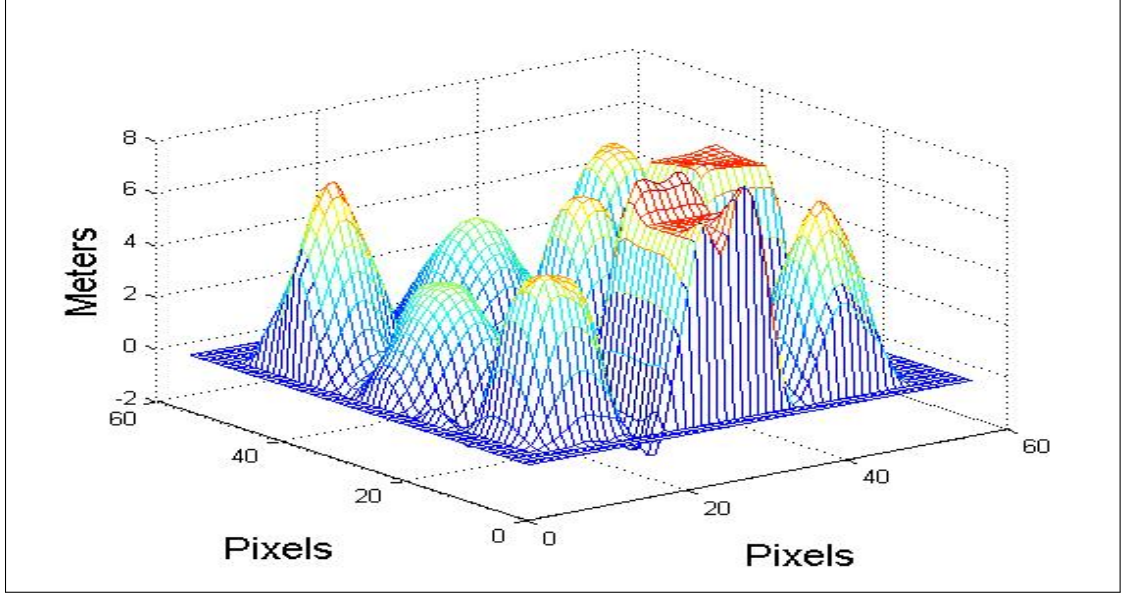


Figure 4.16: Interpolation of target nine using SLR estimates and the bi-Hermite algorithm using the tangent of radians scaled by 0.25 for magnitude.

4.5 Estimation Error

The estimation error was classified using the *mean absolute error* (MAE) metric. The MAE is calculated by [29]

$$MAE(\hat{\theta}) = \frac{1}{MN} \sum_{m=1}^M \sum_{n=1}^N |u(m, n) - u'(m, n)| \quad (4.5)$$

where u' represents the control image and u represents the interpolated image. The MAE expresses the error of the estimates in the units of the variable of interest [29]. The error trends are plotted against the targets and the sampling rates in the time domain. In addition, the estimation error is compared for different pulse width expansion values (τ_g). The points in the figures displayed in this section represent the mean of the MAE calculated over every test ran for that variable.

4.5.1 Target Estimation MAE Analysis. The estimation error for the pulse width expansion is compared in units of radians. The range error calculations are

calculated in meters. The LR and SLR estimation error plots are shown in Figures 4.17 and 4.18.

The averaged MAE calculations for the pulse width expansion peaks for every other target. The peaks occur in targets that contain only a single object. This is consistent with the concerns shown in developing the estimation algorithms in Section 3.3. The slope of the target does not significantly affect the pulse width expansion unless the angle is over 45 degrees. The majority of the pixels in the targets with only one object are flat, which is the reason the plots in Figure 4.17 peak for targets one, three, five, and seven. The estimation algorithm for pulse width expansion clearly struggles with relatively flat targets.

Conversely, the inverse relationship plays out for the range estimations. This follows the intuition that with more objects in the field of view, the more challenging the range estimates will be. The difference between the target range estimate error is highlighted by the SLR plot in Figure 4.18. Also, take note of the difference between the LR and SLR plots. The author does not have a solid theory for the difference between the LR and SLR estimate error shown in Figure 4.18. The continued investigation of the cause for the variance will focus on the different amount of pixels involved with the averaging function of the MAE calculation.

4.5.2 Time Sampling Rate Estimation MAE Analysis. The estimation error plots shown in Figures 4.19 and 4.20 have opposing trends concerning the MAE calculations against the Nyquist scaled sampling rates. The angle estimations get significantly worse as the sampling rate increases. The trend highlights one of the problem areas for the estimation algorithm. As the sampling rate in time increases, the estimator performance decreased to an almost unusable amount. An average MAE calculation of 0.4 radians represents an average estimation error of approximately 23 degrees. Although the performance of the Hermite interpolator suffered, shown by the negative trend in Table 4.7, it was mitigated by the range estimations. The

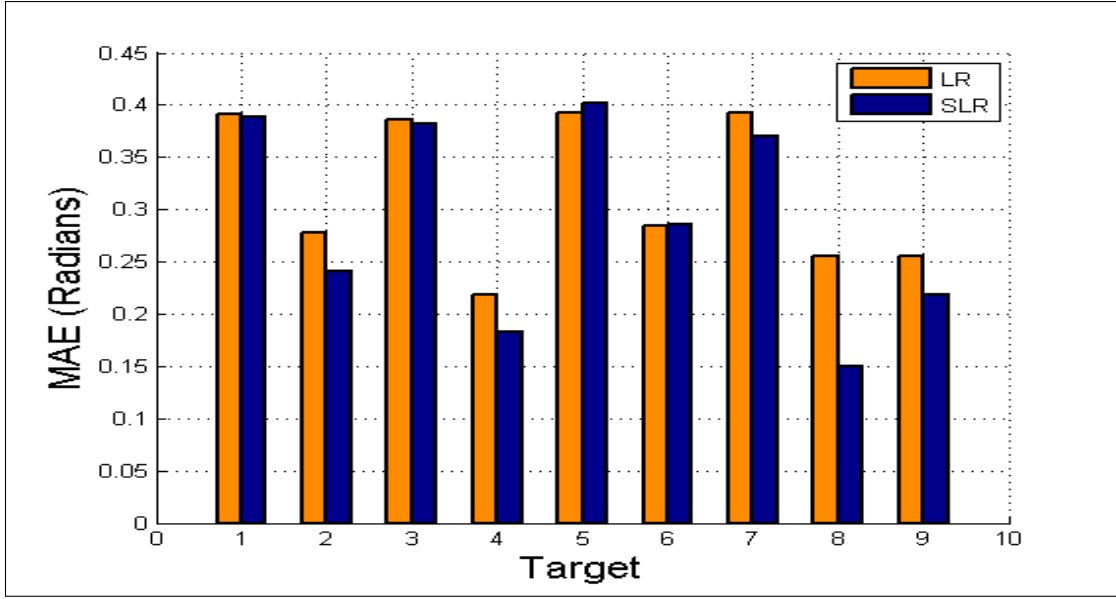


Figure 4.17: Shows average MAE of angle estimations for LR and SLR tests against each target profile.

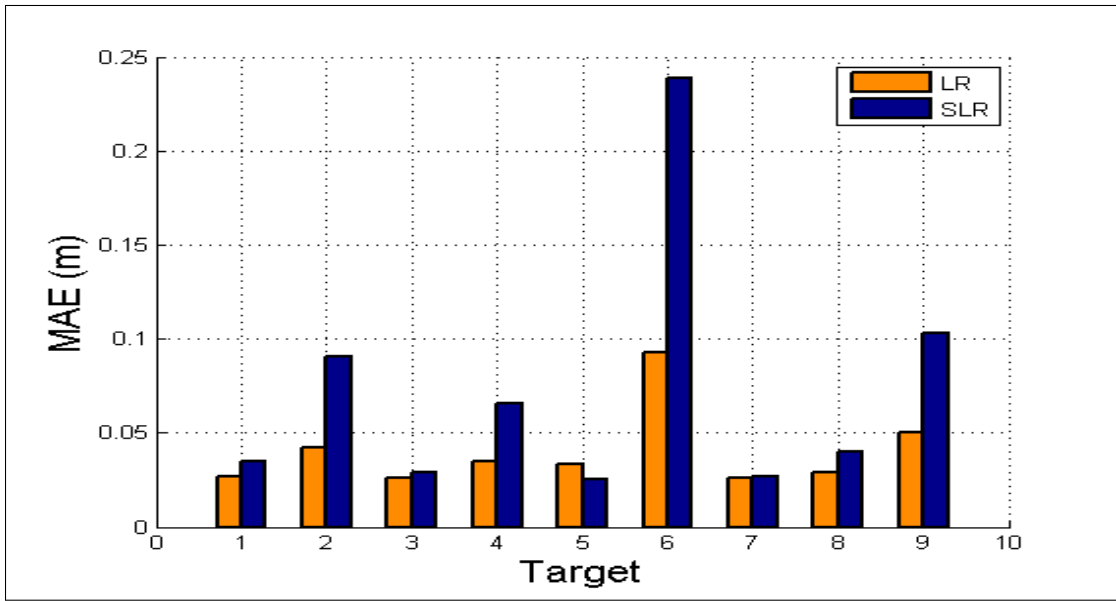


Figure 4.18: Shows average MAE of range estimations for LR and SLR tests against each target profile.

mitigation effects of the range estimations in the bi-Hermite algorithm are described in more detail in Section 4.6.

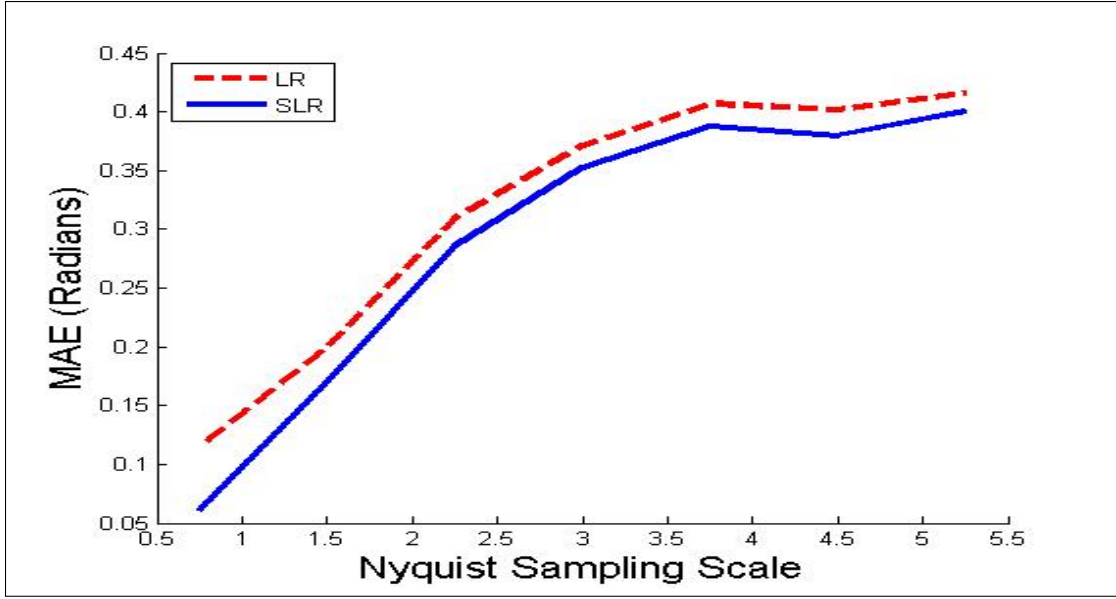


Figure 4.19: Shows error of angle estimation for LR and SLR tests against the Nyquist sampling scale.

The trend in Figure 4.20 shows that as the sampling rate in time increases, the range estimates improve. Although, the trend flattens out at around three times the Nyquist sampling rate. This stabilizing trend is also observed in the plots shown in Figure 4.19.

4.5.3 FWHM Estimation MAE Analysis. The estimation error plots for the FWHM values used in the simulations are shown in Figures 4.21 and 4.22. The error estimates are plotted against the Nyquist sampling scale. The range and angle MAE trends are noticeable again. In addition, it is apparent that the 1 ns FWHM value performs the best when looking at the angle MAE values. The plot shows that the estimator had an easier time discerning the appropriate pulse width expansion when processing a quicker or narrower pulse. The range MAE plots shown in Figure 4.22 show that the best estimation performance occurs with FWHM value of 3 ns. But, when the signal is adequately sampled in the time domain, the difference among the FWHM plots in Figure 4.22 is minimal.

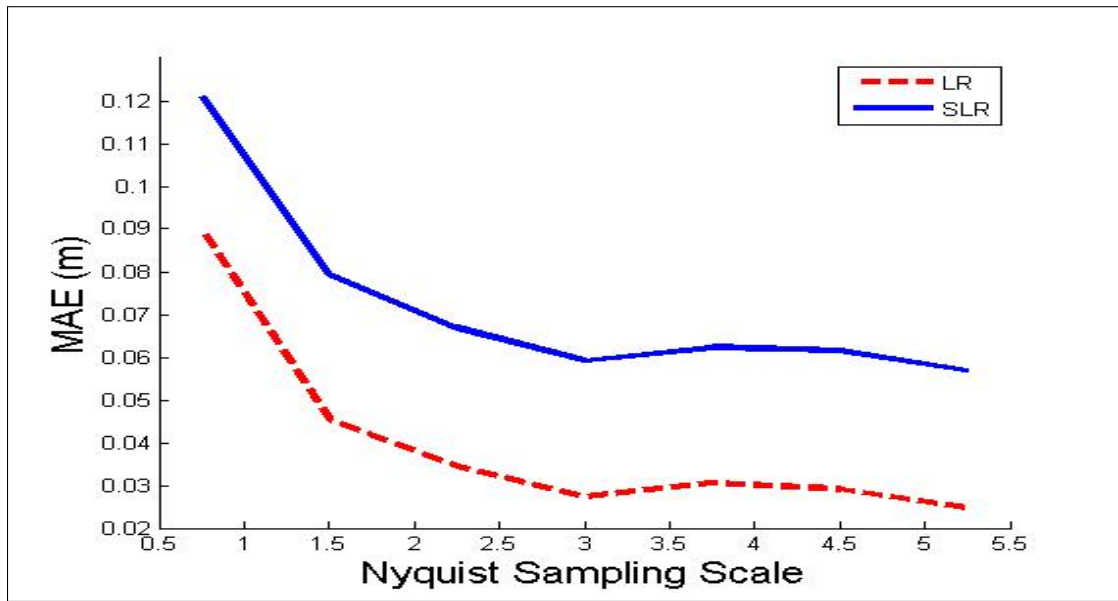


Figure 4.20: Shows error of range estimation for LR and SLR tests against the Nyquist sampling scale.

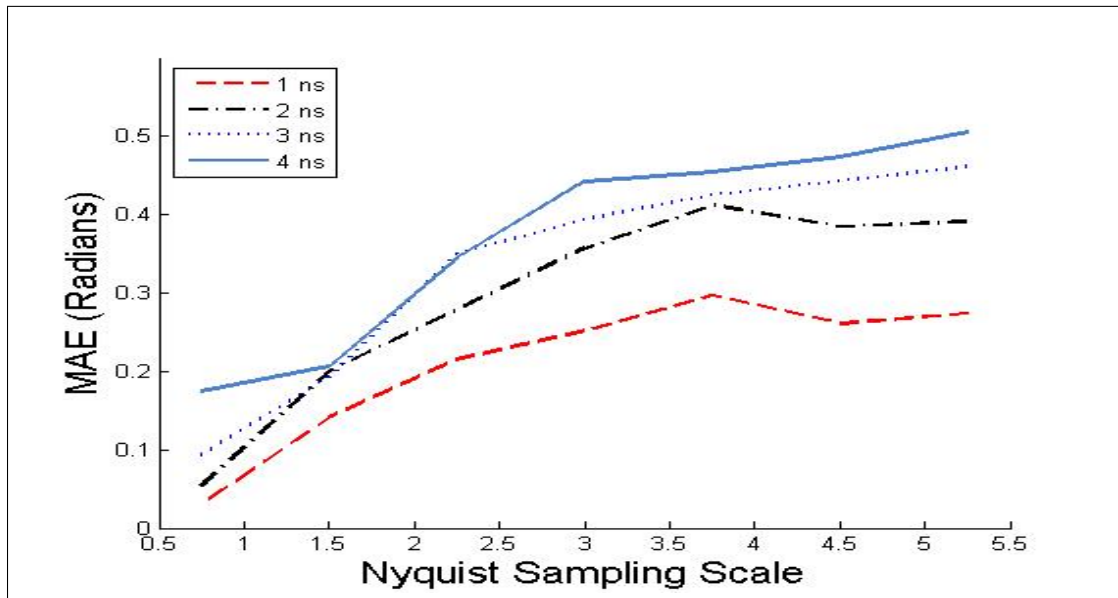


Figure 4.21: Shows error of angle estimation for FWHM (τ_g) tests against the Nyquist sampling scale.

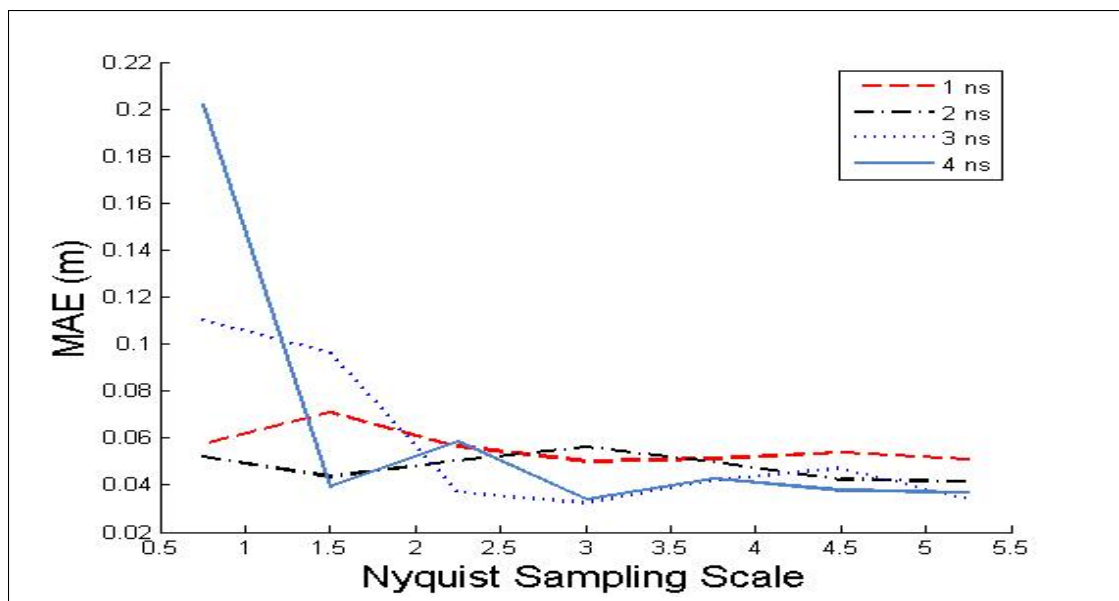


Figure 4.22: Shows error of range estimation for FWHM (τ_g) tests against the Nyquist sampling scale.

4.6 Mitigation of Pulse Width Expansion Error

This section's intent is to explain the resiliency of the Hermite algorithm concerning the error prone estimates of the pulse width expansion. The algorithm for the Hermite interpolator is shown again

$$\begin{aligned}
p_{i,j}(u(x), v(y)) &= \sum_{\Delta i=0}^1 \sum_{\Delta j=0}^1 (f_{i+\Delta i, j+\Delta j}) \alpha_{\Delta i}(u) \alpha_{\Delta j}(v) \\
&+ \sum_{\Delta i=0}^1 \sum_{\Delta j=0}^1 \Delta x_i \left(\frac{\partial f}{\partial x} \right)_{i+\Delta i, j+\Delta j} \beta_{\Delta i}(u) \alpha_{\Delta j}(v) \\
&+ \sum_{\Delta i=0}^1 \sum_{\Delta j=0}^1 \Delta y_j \left(\frac{\partial f}{\partial y} \right)_{i+\Delta i, j+\Delta j} \alpha_{\Delta i}(u) \beta_{\Delta j}(v). \tag{4.6}
\end{aligned}$$

The resiliency of the interpolator concerning poor magnitude gradient estimates comes from the variables Δx_i and Δy_j . The variables concern the x and y direction range estimations. The range estimates introduced less error in the Hermite interpolator algorithm, therefore, in addition to providing direction for the magnitude, it also proved to be a stabilization factor. The egregious angle estimates mostly occurred in the flat portions of the target. Alternatively, the range estimates of the flat sections of the target proved to be the most accurate. Therefore, the majority of the erroneous angle estimates in the flat section were cancelled out by the derivative of the range estimates, typically zero or near zero in the flat sections of the target.

V. Conclusions and Future Work

This section details conclusions that were drawn from the results of this research. These conclusions include the overall performance of the proposed Hermite interpolator as well as the ideal operating conditions for the interpolators. Future research areas are also presented here.

5.1 Conclusions

5.1.1 Hermite Interpolator Performance. The author used T-tests, RMSE comparisons, and surveys to evaluate the performance of the interpolators. By all measures utilized in this study, the Hermite interpolator outperformed the other three interpolators in the majority of the tests. Certain interpolators outperformed the Hermite interpolator in specific cases, but this proved to be the exception and not the rule. The Hermite interpolator developed utilizing the range and pulse width expansion information in the signal provided the most accurate images when compared to the other three mentioned interpolators.

In this limited case, it has been proven that it is possible to measure the pulse width expansion of a laser pulse return and use the information to interpolate a more accurate image. In addition to best measured performance across all of the testing conditions, the Hermite interpolator's performance concerning target nine (multiple shapes) was the best in comparison. The results from target nine are viewed as more important because the target is seen as more realistic and closer to experimental conditions. This result is important because no one has proven that it's possible and beneficial to measure and utilize the available information in the reflected LADAR pulse to increase the resolution of an image of a target.

5.1.2 Ideal LADAR Operating Conditions. In addition to the performance of the Hermite interpolator, the parameters of the LADAR were tested to determine the best operating conditions. Considering the results for the pulse width and range MAE, the ideal sampling rate in the time domain occurs at or just above the Nyquist

sampling rate. This result is ideal when considering the high speeds of the laser presented in this thesis. The increase in performance based on oversampling in the time domain is not justified. The MAE results also showed that the ideal FWHM value for the laser pulse is 1 ns. But, based on the graduated performance of the other three FWHM values, the ideal FWHM value for a LADAR is the fastest pulse width that can be measured.

5.2 *Future Work*

The result found in this study represents the beginning of an endeavor to realize a LADAR system that uses the pulse width expansion of a LADAR pulse to enhance the image of a target. The following sections explain the areas of study that can be explored for research based on the results of this study.

5.2.1 Experimental Results. First, the results found from the simulations in this study should be experimentally tested with LADAR equipment. This would accomplish two goals. First, the experimental tests would confirm the ability of an estimation algorithm to estimate the gradient of the surface of an experimental target. Secondly, the performance of the interpolators using estimates from experimental results could be compared to the theoretical results, possibly confirming the results of this thesis.

5.2.2 LADAR Model Complexity. The LADAR model utilized for this test was relatively simple compared to other potential models. Although this model served a purpose to highlight the intuition behind the performance of the Hermite interpolator, a more robust model is desired for thoroughness. The LADAR model assumes that the equipment and the targets remain motionless and are aligned normal to each other. The LADAR model needs to include the complete BRDF model covered in Section 2.1.3, which includes speckle reflection as well as varied angles of propagation relative to the target plane. Also, a more robust atmospheric and optical model is de-

sired to thoroughly challenge the estimation effort and test the limits of performance of the Hermite interpolator relative to these conditions.

5.2.3 Different LADAR Applications. The application for the LADAR model is intended for small targets at relatively close distances, where the pixel FOVs are relatively small. Another LADAR application that should be considered a candidate for Hermite interpolation is larger systems that image terrain from large distances. This would require at minimum an additional model for the laser field distribution of each pixel because of the relatively large pixel sizes.

5.2.4 Different Image Processing Applications. The Hermite algorithm was only applied to one type of image processing technique, interpolation. There are other image processing techniques that could utilize the pulse width expansion information to generate a better quality image. One potential avenue is the use of both the range and pulse width estimates for comparison against each other to denoise and clean up an image. This method could seek to isolate pixel value outliers based on comparisons of the two estimates.

5.2.5 Test Over Ranges. The author intended to test the interpolators' performance over different target ranges. Although the ranges to the target were changed, the implementation of the tests normalized the differences between the ranges by adjusting the pixel size based on the range. Therefore, data could not be analyzed to compare the difference of the interpolator performances across the different target ranges. The results could have been compared to prior research [9], which suggests that the pulse width expansion decreases as the range to target decreases. This could have lead to a decrease in the performance of the Hermite interpolator.

5.2.6 Thoroughly Test Hermite Interpolator. The discovery of the reason for the Hermite interpolators' success occurred late in the process of this study. More testing is needed to study the optimal implementation of the Hermite interpolator.

Appendix A. Human Subject Paperwork

The human subject paperwork required for the survey is attached on the following pages.



DEPARTMENT OF THE AIR FORCE
AIR UNIVERSITY (AETC)

18 October 2011

MEMORANDUM FOR 711 HPW/IR (AFRL IRB)

FROM: AFIT/ENG (Dr. Martin)
2950 Hobson Way WPAFB, OH 45433-7765

SUBJECT: Request for exemption from human experimentation requirements (32 CFR 219, DoDD 3216.2 and AFI 40-402) for a study on the performance of applied interpolators to create an image of an object

1. The purpose of this study is to determine the performance of various signal processing interpolators on Laser Detection and Ranging (LADAR) returns. The resulting research will be included in the thesis study of one of my students.
2. This request is based on the Code of Federal Regulations, title 32, part 219, section 101, paragraph (b) (2) Research activities that involve the use of educational tests (cognitive, diagnostic, aptitude, achievement), survey procedures, interview procedures, or observation of public behavior unless: (i) Information obtained is recorded in such a manner that human subjects can be identified, directly or through identifiers linked to the subjects; and (ii) Any disclosure of the human subjects' responses outside the research could reasonably place the subjects at risk of criminal or civil liability or be damaging to the subjects' financial standing, employability, or reputation.
3. The following information is provided to show cause for such an exemption:
 - a) Equipment and facilities: No special equipment or facilities will be needed. A survey that is attached will be finished in the near future will be given to the subjects.
 - b) Subjects: The anticipated study population is students who work in the same student section and lab as the experimenter. The students that will be surveyed are mostly in the military with engineering and science backgrounds. Some civilian students with engineering and science backgrounds could be included in the study as well. The potential population of the study group is all male except for one, with age ranging from 22 to 40. This study makes no distinction between gender, age, rank, or any other attributes which might identify one student from another. The expected sample size is around 20 for the survey; the maximum size would be 60, if all students participated. There is no one factor that could potentially bar someone from participation in the study. Enrollment in the study would begin upon the approval from the IRB board.

c) Timeframe: The study is expected to last approximately two weeks, the actual survey should take no longer than five minutes.

d) Data collected: No identifying information will be obtained from the participants. The participants will be given an approximately five minute survey, which is attached. This subject will not collect personal identifiers or specific demographic information.

e) Risks to Subjects: There is little to no risk to participants. The only risk that may exist would be revealing of personal identifying marks on the survey, however every possible effort will be made to separate the surveys from the consent form which the participants will sign. If a subject's future response reasonably places them at risk of criminal or civil liability or is damaging to their financial standing, employability, or reputation, I understand that I am required to immediately file an adverse event report with the IRB office.

f) Informed consent: All subjects are self-selected to volunteer to participate in the interview. No adverse action is taken against those who choose not to participate. Subjects are made aware of the nature and purpose of the research, sponsors of the research, and disposition of the survey results. A copy of the Privacy Act Statement of 1974 is presented for their review.

4. If you have any questions about this request, please contact Richard Martin (primary investigator) – phone 937-255-3636 ext. 4625; E-mail – richard.martin@afit.edu .

Richard K. Martin
Associate Professor of Electrical Eng.
Principal Investigator

Attachments:

1. Survey questions
2. Consent Form

Proposed Survey Questions

Implementation of the Survey:

For the execution of the survey, I will have a printed out control image, which represents the object that was illuminated with a light pulse. Then for comparison, I will have a page of four images that were generated using four different interpolators. Each image will be labeled with a letter. There will be multiple pages of the same four images regarding the different changes that were made for that simulation that produced the four images. The position for each image on every page will be randomized. There will be multiple control images. Each control object that is implemented will be compared in exactly the same way as the first control object.

Survey Question:

Please rank in order from 1 to 4, with 1 being the most accurate and 4 being the least accurate, the following images on page X against control image Y.

Image A:_____ Image B:_____ Image C:_____ Image D:_____

There will be more following questions in the future once the images are generated. They will be a repeat of the first question, with changes to “page X” or “control image Y.”

STUDENT CONSENT FOR PARTICIPATION IN RESEARCH

A study to examine the performance of image interpolators when implemented on LADAR returns from certain objects.

PURPOSE AND BACKGROUND

Jeramy Walter Motes, a graduate student in the ENG department at the Air Force Institute of Technology, is conducting a research study to examine the performance of image interpolators when applied to Laser Range and Detection (LADAR) returns generated by illuminating certain objects. I am being asked to participate in this study because I am a student at AFIT.

PROCEDURES

If I agree to be in the study, the following will happen:

I will complete one survey which will take approximately five minutes. Only those participants with a signed consent form may participate.

RISKS/DISCOMFORTS

There are no foreseen risks in participating in this study.

CONFIDENTIALITY

Participation in research may involve a loss of privacy, but information about me will be handled as confidentially as possible. The researcher, Jeramy Walter Motes, will have access to information about me. . Other participants involved in this study will not receive information about me. Other faculty or senior members of AFIT will not receive information about me. My name will not be used in any published reports about this study.

BENEFITS

There will be no direct benefit to me from participating in this study.

QUESTIONS

If I have questions about this research study, or have a research-related injury to report, I can contact the researcher Jeramy Walter Motes at 850-582-4727. If I would like a copy of the group (not individual) results of this study, I can contact Jeramy Walter Motes. It is estimated that these results will be available on or after 20 Nov 2011.

CONSENT

I will be given a copy of this consent form to keep.

PARTICIPATION IN RESEARCH IS VOLUNTARY. I am free to decline to be in this study, or to withdraw from it at any point. My decision as to whether or not to participate in this study will have no influence on my present or future status as a student athlete in this program.

If I agree to participate I should sign below.

Date

Signature of Study Participant

Date

Signature of Person Obtaining Consent



**DEPARTMENT OF THE AIR FORCE
AIR FORCE INSTITUTE OF TECHNOLOGY
WRIGHT-PATTERSON AIR FORCE BASE OHIO**

21 Oct 2011

MEMORANDUM FOR DR. RICHARD K. MARTIN

FROM: Jeffrey A. Ogden, Ph.D.
AFIT IRB Research Reviewer
2950 Hobson Way
Wright-Patterson AFB, OH 45433-7765

SUBJECT: Approval for exemption request from human experimentation requirements (32 CFR 219, DoDD 3216.2 and AFI 40-402) for a study on the performance of applied interpolators to create an image of an object.

1. Your request was based on the Code of Federal Regulations, title 32, part 219, section 101, paragraph (b) (2) Research activities that involve the use of educational tests (cognitive, diagnostic, aptitude, achievement), survey procedures, interview procedures, or observation of public behavior unless: (i) Information obtained is recorded in such a manner that human subjects can be identified, directly or through identifiers linked to the subjects; and (ii) Any disclosure of the human subjects' responses outside the research could reasonably place the subjects at risk of criminal or civil liability or be damaging to the subjects' financial standing, employability, or reputation.
2. Your study qualifies for this exemption because you are not collecting sensitive data, which could reasonably damage the subjects' financial standing, employability, or reputation. Further, the demographic data you are collecting, if any, and the way that you plan to report it cannot realistically be expected to map a given response to a specific subject.
3. This determination pertains only to the Federal, Department of Defense, and Air Force regulations that govern the use of human subjects in research. Further, if a subject's future response reasonably places them at risk of criminal or civil liability or is damaging to their financial standing, employability, or reputation, you are required to file an adverse event report with this office immediately.

JEFFREY A. OGDEN, PH.D.
AFIT Research Reviewer

Bibliography

1. O. Steinvall, U. Soderman, S. Ahlberg, M. Sandberg, D. Letalick, and E. Jungert, "Airborne Laser Radar: Systems and Methods for Reconnaissance and Terrain Modeling," in *SPIE 3707*, April 1999, p. DOI:10.1117/12.351338.
2. L. Martin, "Low Cost Autonomous Attack System," 2006, [Online]. Available at <http://defense-update.com/products/1/locaas.htm>. [Accessed 23-September-2011].
3. A. V. Oppenheim and R. W. Schaffer, *Discrete-Time Signal Processing*. Upper Saddle River, NJ: Pearson, 2010.
4. R. T. Smith and R. B. Minton, *Calculus*. New York, NY: McGraw-Hill, 2002.
5. P. J. Davis, *Interpolation and Approximation*. Mineola, NY: Dover Publications, 1963.
6. B. P. Lathi, *Linear Systems and Signals*. New York, NY: Oxford University Press, 2005.
7. D. P. Mitchell and A. N. Netravali, "Reconstruction Filters in Computer Graphics," *Computer Graphics*, vol. 22, pp. 221–228, August 1988.
8. O. Steinvall, "Effects of Target Shape and Reflection on Laser Radar Cross Sections," *Applied Optics*, vol. 39, no. 1, pp. 4381–4391, August 2000.
9. S. Johnson, "Range Precision of LADAR Systems," Ph.D. dissertation, Air Force Institute of Technology, 2950 Hobson Way, WPAFB, OH 45433-7765, 2008.
10. Q. Zheng, S. Z. Der, and H. I. Mahmoud, "Model-Based Target Recognition in Pulsed Ladar Imagery," *IEEE Transactions on Image Processing*, vol. 10, no. 4, pp. 565–572, April 2001.
11. S. Cain and R. D. Richmond, *Direct-Detection LADAR Systems*. Bellingham, Washington: SPIE, 2010.
12. K. D. Neilson, "Signal Processing on Digitized Ladar Waveforms for Enhanced Resolution on Surface Edges," Master's of Science, Utah State University, Logan, Utah, 2011, [Online]. Available at <http://digitalcommons.usu.edu/cgi/viewcontent.cgi?article=1879&context=etd>. [Accessed 29-June-2011].
13. T. R. Chevalier and O. K. Steinvall, "Laser Radar Modeling for Simulation and Performance Evaluation," in *SPIE 7482*, 2009, p. DOI:10.1117/12.830467.
14. E. Hecht, *Optics*. San Francisco, CA: Addison Wesley, 2001.
15. R. L. Lucke, "Rayleigh-Sommerfeld Diffraction vs Fresnel-Kirchhoff, Fourier Propagation, and Poisson's Spot," NRL/FR/7218-04-10,101, December 2004,

[Online]. Available at <http://www.dtic.mil/cgi-bin/GetTRDoc?AD=ada429355>. [Accessed 29-September-2011].

16. J. Goodman, *Introduction to Fourier Optics*. Greenwood Village, CO: Roberts and Company, 2005.
17. J. H. Shapiro, "Target-reflectivity Theory for Coherent Laser Radars," *Applied Optics*, vol. 21, no. 18, pp. 3398–3407, September 1982.
18. O. Steinvall and T. Carlsson, "Three-Dimensional Laser Radar Modeling," in *SPIE 4377*, 2001, p. DOI:10.1117/12.440110.
19. R. Richmond, S. W. Henderson, and C. P. Hale, "Atmospheric Effects on Laser Propagation Comparisons at 2 and 10 Microns," in *SPIE 1633*, 1992, pp. 74–85.
20. J. Goodman, *Statistical Optics*. USA: John Wiley and Sons, 1985.
21. H. M. Kwon, "Optical Orthogonal Code-Division Multiple-Access System—Part I: APD Noise and Thermal Noise," *IEEE Transactions on Communications*, vol. 42, no. 7, pp. 2470–2479, July 1994.
22. G. Lachs, "Theoretical Aspects of Mixtures of Thermal and Coherent Radiation," *Physical Review*, vol. 138, no. 4B, pp. 1012–1016, May 1965.
23. D. G. Bailey and K. T. Gribbon, "A Novel Approach to Real-Time Bilinear Interpolation," in *Electronic Design, Test and Applications 2004*, 2004, p. DOI:10.1109/DELTA.2004.10055.
24. A. K. Jain, *Fundamentals of Digital Image Processing*. Upper Saddle River, NJ: Prentice Hall, 1989.
25. Xiaowei, Y. Jiahao, and Deng, "Imaging Simulation for 3-D Laser Radar Based on Target Model," in *SPIE 1633*, 2009, p. DOI:10.1117/12.806506.
26. C. Gronwall, O. Steinvall, F. Gustafsson, and T. Chevalier, "Influence of Laser Radar Sensor Parameters on Range-Measurement and Shape-Fitting Uncertainties," *Optical Engineering*, vol. 46, no. 10, pp. 1–11, October 2007.
27. B. T. Deas, "Pulse Shape Correlation for Detection and Ranging LADAR," Master's of Science, Air Force Institute of Technology, Dayton, OH, 2010.
28. R. R. Wilcox, *Applying Contemporary Statistical Techniques*. Elsevier, Oxford, UK: Academic Press, 2003.
29. C. J. Willmott and K. Matsuura, "Advantages of the Mean Absolute Error (MAE) Over the Root Mean Square Error (RMSE) in Assessing Average Model Performance," *Climate Research*, vol. 30, pp. 79–82, December 2005.

REPORT DOCUMENTATION PAGE					<i>Form Approved</i> <i>OMB No. 0704-0188</i>	
The public reporting burden for this collection of information is estimated to average 1 hour per response, including the time for reviewing instructions, searching existing data sources, gathering and maintaining the data needed, and completing and reviewing the collection of information. Send comments regarding this burden estimate or any other aspect of this collection of information, including suggestions for reducing this burden to Department of Defense, Washington Headquarters Services, Directorate for Information Operations and Reports (0704-0188), 1215 Jefferson Davis Highway, Suite 1204, Arlington, VA 22202-4302. Respondents should be aware that notwithstanding any other provision of law, no person shall be subject to any penalty for failing to comply with a collection of information if it does not display a currently valid OMB control number. PLEASE DO NOT RETURN YOUR FORM TO THE ABOVE ADDRESS.						
1. REPORT DATE (DD-MM-YYYY) 22-03-2012		2. REPORT TYPE Master's Thesis		3. DATES COVERED (From — To) Sept 2010 — Mar 2012		
4. TITLE AND SUBTITLE LADAR Range Image Interpolation Exploiting Pulse Width Expansion				5a. CONTRACT NUMBER 5b. GRANT NUMBER 5c. PROGRAM ELEMENT NUMBER 5d. PROJECT NUMBER 12G292U 5e. TASK NUMBER 5f. WORK UNIT NUMBER		
6. AUTHOR(S) Motes, Jeramy W., 2d Lt, USAF				8. PERFORMING ORGANIZATION REPORT NUMBER AFIT/GE/ENG/12-30		
7. PERFORMING ORGANIZATION NAME(S) AND ADDRESS(ES) Air Force Institute of Technology Graduate School of Engineering and Management (AFIT/ENG) 2950 Hobson Way WPAFB OH 45433-7765				10. SPONSOR/MONITOR'S ACRONYM(S) AFOSR/RSE		
9. SPONSORING / MONITORING AGENCY NAME(S) AND ADDRESS(ES) Kent Miller Air Force Office of Scientific Research, ATTN: Kent Miller-RSE 875 North Randolph Street, Room 3112 Arlington, VA 22203 COMM: (703) 696-8481 kent.miller@afosr.af.mil				11. SPONSOR/MONITOR'S REPORT NUMBER(S)		
12. DISTRIBUTION / AVAILABILITY STATEMENT APPROVED FOR PUBLIC RELEASE; DISTRIBUTION UNLIMITED.						
13. SUPPLEMENTARY NOTES This material is declared a work of the U.S. Government and is not subject to copyright protection in the United States.						
14. ABSTRACT <i>Laser Detection and Ranging</i> (LADAR) systems produce both a range image and an intensity image by measuring the intensity of light reflected off a surface target. When the transmitted LADAR pulse strikes a sloped surface, the returned pulse is expanded temporally. This characteristic of the reflected laser pulse enables the possibility of estimating the gradient of a surface. This study estimates the gradient of the surface of an object from a modeled LADAR return pulse that includes accurate probabilistic noise models. The range and surface gradient estimations are incorporated into a novel interpolator that facilitates an effective <i>three dimensional</i> (3D) reconstruction of an image given a range of operating conditions. The performance of the novel interpolator is measured by comparing the reconstruction effort against the performance of three common interpolation techniques: linear, spline, and sinc.						
15. SUBJECT TERMS LADAR, Image Resolution, Interpolation, Pulse Width Expansion						
16. SECURITY CLASSIFICATION OF:			17. LIMITATION OF ABSTRACT UU	18. NUMBER OF PAGES 98	19a. NAME OF RESPONSIBLE PERSON Richard K. Martin, (ENG)	
a. REPORT U	b. ABSTRACT U	c. THIS PAGE U			19b. TELEPHONE NUMBER (include area code) (937) 255-3636, x4625; Richard.martin@afit.edu	